Addis Ababa Univeristy

Insititution of Technology

School of Civil and Environmental Engineering

Department of Geomatic and Geodesy Msc Program

GROUND DEFORMATION ANALYSIS USING PERSISTENT-SCATTER INTERFEROMETRY: A CASE STUDY OF ERTA ALE VOLCANO IN AFAR ETHIOPIA

BY

TILAYE SEWNET GELA

ID No GSR/4950/14

ADVISOR: ANDENET ASHAGRIE (PHD)

Thesis is submitted to school of graduate studies of addis ababa university in partial fulfilment of the requirement of the degree of masters of science in geodesy and geomatics program (specialization geodesy)

February 2024

Addis Ababa Ethiopia

Declaration

I the undersigned, declare that the thesis work titled "**Determining Ground Surface Deformation at Erta Ale Volcano and Assessing Lava Lake Reservoir Northern Afa**r and that it has not been submitted for a degree at any other university. I properly acknowledge for all sources of materials used for this thesis work.

Tilaye Sewnet Gela ID No GSR4950/14

Feb 9, 2024

Name of Student Date Signature

I at this moment certify that I have read and evaluated this MSc thesis

Dr. Andenet Ashagrie Feb 10,

Name of Supervisor Signature Date

Approval Sheet

Addis Ababa Institute Of Technology

School Of Civil And Environmental Engineering

The undersigned have examined the thesis entitled "Ground Deformation Analysis Using Persistent-Scatter Interferometry: A Case Study of Erta Ale Volcano In Afar Ethiopia presented by Tilaye Sewnet, a candidate for the Degree of Master of Science in Geodesy and Geomatics with a specialization in Geodesy and at this moment certify that it is worthy of acceptance.

Board of Examiners Committee:

1. Andenet Ashagrie (Phd) Feb 10, 2024

Advisor Signature Date

Sintayehu Abie 09/02/24

Erternal Examiner Signature Date

Andnet Nigussie Feb 9, 2024

Snternal Examiner Signature Date

Sintayehu A. 09/02/2024

Signature Date

Abrham Gebre (Dr.)
Dean, School of Civil &
Environmental Engineering

Addis Ababa University Addis Ababa Institute of Technology
Director of Postgraduate Program

Chairperson

ii

Abstract

This research endeavors to ground surface deformation analysis using Persistent scatter interferometry at Erta Ale volcano and assessing its Lava Lake reservoirs in northern Afar Ethiopia spanning the period from 2017 to 2022, using Sentinel-1A data. Erta Ale is an active volcano located tectonically at the triple divergent junction of the Arabian, Nubian, and Somalian divergent plates. Geological setting of Erta Ale is highly extended and thin crust layer which is additional factor to Era Ale volvcanic activity. Studying the ground deformation of actively erupted volcanoes at the local level is one way of monitoring the continental refits. In this study, 26 sentinel-1A descending single look complex (SLC) SAR data are the main input for the study. SAR data covers large areas that enables to generate densified Ground control points to assess surface displacement at active volcano area. The latest InSAR processing method, PS-InSAR, is used to process SAR data. The commercial software SARPROZ used to process and analyze data in PS-InSAR techniques. Atmospheric phase error are removed by the amplitude-phase scattering (APS) method in this method. In the subsidence area, maximum horizontal and vertical displacement are~143±1.2674 mm and~91.89mm, respectively. Areas including Bora Ale and areas in the NW of the north pits are continuously subsiding. In the Northeast, the deforming rate of subsidence is 13.76mm per year, resulting in ~12mm of ground contraction and vertical deflation ~40m. Between Ali Bagu and Boral areas, there are some boreholes and temporary cracking that cause depression of the earth's surface. uplifting area is ~60.23 ±1.2674 and ~93.04 mm, respectively, in the SW direction, resulting in horizontal extension of PSC ~12cm. North pit Lava Lake magma has decreased in area from the February2017 to December 2022 is ~0.061723km^2 to ~0.036983km^2.

Keywords: *Atmospheric phase scattering, Ground deformation, Persistent-scatter intefreometry,Ssubsidence, Uplift*

Acknowledgements

Primarily, I want to express my gratitude to God for all I have faced during this study. I thank my father, Sewnet Gela, and priest, Girma Animut, whom I lost during this study.

I also thank my family and wife, Alemnesh Animut, for their unlimited support. I must give special and heartfelt thanks to Dr. Andenet Ashagrie, my advisor and coordinator of geodesy and geomatics at Addis Ababa University Institution of Technology, who encouraged me to work on this research title and followed me with continuous guidance, support, and encouragement throughout, and for devotedly contributing to the thesis's success. I want to thank my colleague from Debrebirhan University, Andinet Nigusise (PhD), for his valuable encouragement, comments, and suggestions during processing and report writing. I also thank Daniele Perissin (PhD) and the entire SARPROZ admin team for their warrants of license for providing the SARPROZ license and tutorial manual.

Abbreviation

AOI	Area of interest
APS	Atmospheric phase scattering
ATI	Across Track interferometry
CSV	Comma separated vale
DEM	Digital Elevation model
D-InSA	Deferential interferometric synthetic aperture radar
EAR	East African Rift
EAVS	Erta Ale Volcano system
ESA	European Space Agency
GCP	Ground control point
GIS	Geographic information system
GPS	Global positioning system
IPD	Interferometric phase difference
IW	Interferometry wide
QGIS	Quantitative geographic information system
RAR	real aperture radar
RMS	Root mean square
RSR	Red Sea Rift
LOS	Line of sight
MER	Main Ethiopian Refit
NASA	National Aeronautics and Space Administration.
NLl	None local

NNW	North-Northwest
PSC	Stable point candidate
PSI	Persistent scatter Interferometry
S-1A	Sentinel 1 A
SCR	Single clutter ratio
SLC	Single look complex
SRTM	Shuttle radar topography mission
TOPS	Terrain observation by progressive scan
UTM	Universal traverse Mercator3
VH	Vertical transmission to the horizontal receiver
VV	Vertical transmission to the vertical receiver
WGIS	World Geographic Information System

Contents

List of Figures

List of Table

Chapter One

1. Introduction

1.1 Background of the Study

This research endeavors to ascertain ground surface deformation and assessing its Lava Lake reservoirs at Erta Ale volcano northern Afar Ethiopia spanning the period from 2017 to 2022, using Sentinel-1A data. There are few active volcanos in the world. And among some volcanos in Africa Erta Ale is found in Ethiopia. Volcanic activity causes volcanic eruptions and rifting events.Volcanic activity, encompassing eruptions and rifting events, induces deformation concurrent with magma accumulation and eruption occurrences. Erta Ale, situated in the northern Afar region of Ethiopia, constitutes one of the most active volcanoes globally within a volcanically active rift system.

It is one of the few areas in the world that offers capture the ongoing process of continental break-up associated with a mantle plume (Wolfenden et al. 2004). Geologically it is a highly extended and thin crust, 25 to 15 km thick from south to north, its thickness larger that is 40km thick crust below the Ethiopian Plateau (Hammond et al. 2011; F. Zwaan et al. 2020).

Tectonically positioned at the Afar triple junction, Erta Ale is emblematic of divergent motions between the Arabian, Nubian, and Somalian plates along the Red Sea, Gulf of Aden. And it is located at EAR, providing valuable implications that Erta Ale is good implication for understanding these tectonic dynamics (Kumar, Legendre, and Huang 2021; Frank Zwaan et al. 2020). Erta Ale exhibits gradual deformation in EAVS that represents the southern end of the RSR; thus signifying its role as an indicator of the impending continental breakup (Zwaan et al., 2019).

The investigation of active volcano deformation serves as a means to explore volcanic activity and the geophysical characteristics of deep pressure sources beneath the Earth's surface. Changes in pressure within the magma chamber, attributed to magma flow, lead to inflation and deflation of the magma reservoir beneath the volcano. Deformation manifestations on the surface, such as terrain displacements, are influenced by volume and geometry changes in the magma chamber. This study focuses on Erta Ale volcano and its surroundings, addressing the ongoing challenges associated with ground deformation. Previous research suggests fluctuations in the Lava Lake reservoir over different years (Doubre et al., 2017; Kumar et al., 2021; Moore et al., 2019, 2020; l, 2005; Xu, 2020;

Zwaan et al., 2019). Recent reports note consistent thermal anomalies in the south pit lava lake from October 2021 to May 2022, while thermal activity in the north pit crater exhibited more variability (BGVN 47:05). The observed behavioral changes persist through November 2022, motivating further investigation into ground deformation at Erta Ale. From a geodesy standpoint, the impact of crustal motion on permanent GPS is less pronounced than at the active volcano itself due to the scarcity and limited functionality of GPS stations in Ethiopia. Pointwise velocity deformation using GPS data necessitates interpolation, introducing additional errors. Therefore, to comprehensively study volcano-induced deformation over time, SAR data is employed. SAR enables the detection of sub-centimeter-level surface changes over large areas within a given timeframe, offering a potent alternative to ground-based techniques that are time-consuming and financially burdensome (Guarango, 2022).

The pointwise velocity deformation using GPS data is using interpolation that causes more error. To study the deformation due to volcano with time series, we used the SAR data. It can determine the deformation of large areas bellow centimeter level in time span. This is a powerful method for areas where ground-based techniques are time consuming and need large cost (Grandin et al. 2010). InSAR emerges as a key satellite-based geodetic technique for monitoring ground deformation, as it can detect sub-centimeter-level surface changes annually. Time-series displacement changes at active volcanoes are challenging to ascertain through ground survey methods such as leveling and traditional survey instruments. These ground based survey is not cost effective, and very time consuming even though if it is possible. Consequently, the utilization of advanced space geodetic techniques, particularly InSAR, is deemed the most effective approach, utilizing freely available satellite data. The PSI method, applied with APS removal, is deemed suitable for processing SAR data. Some of the studies are conducted to evaluate the continental plate deformation and the consequence of the magma stored at Erta Ale. Localized studies of ground deformation at Erta Ale's volcanic eruption site prove more effective than broader regional or continental investigations, as evidenced by a threefold larger deformation magnitude observed in local studies compared to continental studies. As (Moore et al. 2019) underscores the efficacy of local-scale investigations in elucidating the intricacies of active volcano deformation. Geological thickness, its location at meeting point of three divergent tectonic plate and the continuity of the refitting system until 2022; these and other evidence are the main to study the ground deformation. In general InSAR data are more precise value than GPS point wise velocity deformation.

1.2 Statement of Problem

Erta Ale volcano stands out as one of the world's few active volcanoes, situated within the volcanically active rift system in Ethiopia. Its unique global location provides an opportunity for scholars to examine the ongoing continental break-up process associated with a mantle plume (Wolfenden et al. 2004). Recently, in January 2017, the volcano experienced a reactivation event, leading to a substantial overflow of magma onto the surface. The withdrawal of magma may induce changes in the active lava lake reservoir area.

Furthermore, various research journals have reported fluctuations in the Lava Lake reservoir over different years (Doubre et al. 2017; Moore et al. 2019; Xu 2020). The spread of lava on the ground is expected to result in surface deformation, emphasizing the need for continuous monitoring of the volcano. The status of the lava lake reservoir exhibits temporal variations. Previous studies predominantly employed pointwise GPS by interpolation method to evaluate displacement at active volcanos. Others use SAR data to assess deformation during reactivation, focusing on crustal deformation. However, such approaches yield less accurate values than InSAR, particularly at the local level. Other scholars focus on the continental crustal deformation rather than local ground deformation. Crustal deformation in regional; level shows less displacement value than local study.

The volcanic eruption at Erta Ale significantly outpaces the deformation rates associated with continental rifts or tectonic plate motions, with local studies proving more accurate than broader regional assessments. According to local time-series deformation is three times greater than continental deformation within the same Erta Ale volcano area. Reports from the World Volcano Program indicate fluctuating thermal intensities in the south and north pits of Erta Ale, signifying varying states of the Lava Lake. These thermal fluctuations contribute to the displacement of molten magma, resulting in deformation in the volcano pits and their surrounding areas. Consequently, understanding and monitoring these volcanic activities are crucial for comprehending the dynamics of Erta Ale and its impact on the surrounding environment.

1.3 Objective of study

1.3.1 General Objective

The general objective is ground deformation analysis using persistent-scatter interferometry in case study of Erta Ale volcano from February 2017 to December 2022.

1.3.2 Specific Objective

This research has the following objectives:

1. Analyzing horizontal displacement of Erta Ale over the past six years.
2. Detect vertical deformation, along with its velocity, within a 20 km radius around the volcano for the last six year period.
3. Assess the status of the Lava Lake reservoir by comparing interferograms from 2017 and 2022, along with the corresponding shape file maps for those years.

1.4 Research question

The research aims to address the core purpose of the study by providing answers to the identified problem

1. What is the linear and vertical displacement of Erta Ale volcano for the last six years?
2. What is the status of the Lava Lake reservoir in two pits?
3. What is the rate of deformation at Erta Ale?

1.5 Scope of Study

This study was conducted in northern Afar, Ethiopia, focusing on the Erta Ale volcano ground surface deformation within a 20 km radius. This radius was chosen to cover a small but significant area characterized by prominent active refitting activities. The primary purpose of the study is to evaluate horizontal and vertical surface displacement in the Erta Ale volcano and its surrounding areas from January 2017 to December 2022, utilizing Sentinel-1A with descending SLC SAR data using the latest PSI processing method. Additionally, the study investigates area changes in the lava lake pits during the specified study period.

The research aims to determine deformation rates per year and presents resampled displacement in both linear and height dimensions to identify periods of increased deformation. In the final assessment of the volcano, changes in the lava lake reservoir area are examined using interferograms of the study year beginning time and end of the study year with the same phase contours.

1.6 Significance of the Study

This thesis study focuses on analyzing ground surface deformation at Erta Ale, an active volcano, and its surrounding areas within a 20 km radius. The research provides insights into both vertical and horizontal displacement, along with the deformation rates of the volcano and its vicinity. This study serves as a valuable reference for researchers intending to conduct further investigations at Erta Ale, offering a foundational understanding of the deformation patterns.

Researchers interested in studying deformation at Erta Ale volcano can use this thesis as a reference base, enhancing their comprehension of the geological dynamics in the region. The findings and analysis presented in this paper contribute to the existing body of knowledge related to the deformation processes at Erta Ale. Moreover, authorities and relevant bodies in the Afar region to formulate strategies for protecting against environmental hazards associated with the volcano over the past six years can utilize the information presented in this study. This research is significant not only for its scientific contribution but also for its potential practical applications in managing and mitigating risks related to volcanic activity in the region.

1.7 Limitations of the Study

The research encountered several challenges throughout its course, including limitations in computer processor capabilities, storage capacity, internet connectivity issues, and technical training gaps in SAR data processing. Some of these challenges were successfully addressed, while others proved beyond the scope of resolution. One particularly formidable obstacle was the difficulty in accessing commercial software capable of processing extensive time series data.

SARPROZ software was employed for SAR data processing during the study. However, a critical limitation was identified the software processes data within only a 20 km radius. Consequently, the study results depict only narrow areas around the active volcano, limiting the broader understanding of ground deformation.

Another hindrance to the study was related to security concerns within the country, making it challenging to physically observe the study area. The absence of direct physical observation impedes the ability to visually assess and verify the state of the volcano and its surroundings. This limitation complicates the generalization of findings, particularly concerning subtle fault lines in the southwestern region of Erta Ale and their origins. It is essential to understand that this thesis primarily focuses on ground deformation from a geodesy and geomatics perspective. To comprehensively understand volcanic eruptions, further research should encompass multiple disciplines, including geology, geophysics, geochemistry, volcanology, and others, integrating their findings for a holistic understanding. These disciplines to answer and model the volcanic deformation and justify why the area of the active volcano decrease; however the thermal intensity is still vary.

1.8 Thesis Outline

This paper is organized into five chapters, each addressing specific topics in detail. Chapter 1 introduces the study area background information, outlines the main purpose of the study in additionally states the problem statement, and specifies the study's objectives. To achieve this purpose what data and method is used to process such data will be discussed. The geographical location's significance and limitations are elaborated upon extensively. Chapter 2 comprises a literature review of the study area and relevant theories about the methodologies. It defines some terms that are necessary and used in this study. The discussion includes what data processing techniques are used for previous study, with a clear elucidation of necessary theories that are used to clarify the data processing techniques from the last decade to this study. Chapter 3 details description of the methodology and method of the thesis, providing the input data, and the processing and analyzing techniques. Clear procedures on how to precisely process the data are presented. Chapter 4 focuses on the results and discussion, presenting all relevant findings in an appropriate format. Each results are discussed to interpret the map, tables or any outputs. Maps requiring clarification are discussed by justifying and judging using the scientific knowledge that are discussed under discussion sub section. Finally, Chapter 5 presents the conclusion and recommendations. Results are generalized and summarized, leading to recommendations for concerned bodies based on the study's findings.

Chapter Two

2. Literature Review

Literature review is the selected articles and journals that different researcher has done about the study area. It enable to us to why the problem is still continued, what data and methods they used and other necessary information are gathered about Erta Ale volcano deformation. This reference journals and articles enable us to select the method of research. It also elaborates the theories of InSAR technique, types of SAR processing and error budget in SAR data.

2.1 Background of the Volcanic Eruption

Volcanoes are the cause for permanent deforming the surface of the earth as observed in active and/or fossil examples on the ground (Gudmundsson 2020). Volcanic eruptions always cause ground surface deformation horizontally and vertically during magma accumulation and erupting time (Moore et al. 2019). According to (Xu 2020) the eruption can lead to various erupting styles characterized by differences in the size, strength, and frequency of volcanic activities.

Deformation can formed before or after the eruption and may be uplift or subsidence according to the magma. There are two sources of deformation from volcanos; one is deeper source causing the volcano-wide deformation and other is shallower dike-like source responsible for the deformation close to the northern caldera. These displacement will be uplifted due to the lava is overflowed to the surrounding areas during refitting time, and subsidence occurs when the lava flows underground crust and due to withdrawal of the magma. The velocity of rifting activity of volcano deformation happened after eruption time are dependent on the magmatic processes occurring at depth and the rheology of the crust and magma (Hamling et al. 2014).

2.1.1 Geological Setting of Afar

Geological setting is the core cause of the regional seismicity that play main role of active volcanos like Erta Ale. Seismicity causes the magma motion under the crust. The first geology of Afar including Erta Ale was studied since January 1968, when a French-Italian team led by Giorgio Marinelli and Haroun Tazieff, of which Jacques Varet and I were young members, initiated the systematic geological exploration of Afar along the axis of the depression of some active volcanic ranges displaying magmatic and tectonic features. This is suggesting that they were oceanic structures, an indication of continental laceration (Varet 2018). The northern Afar merges to the south in southwestern and the east-central Afar the NNW-trending structural grain related to the Red Sea flexes anti-clockwise to a more E–W trend. East and central Afar is integrate with the Danakil Block where active volcano is found and the Tendaho-Gobaad discontinuity in the west and southwest. As (Beyene and Abdelsalam 2005) describes geology of Afar is dominated by NW-trending grabens and horsts between spreading to Manda Hararo-Gobaad and in NW. The Afar depression in the northern has a highly extended thin crust, 25 to 15 km thick from south to north, its thickness larger that is 40km thick crust below the Ethiopian Plateau (Hammond et al. 2011; F. Zwaan et al. 2020). This thickness of crust has the significant role for the active volcano the crustal magma motion to come out to lava lake pits.

Afar depression is different from MER in geological setting, Mio-Pliocene silicic volcanism is closely composed of fissural basaltic products during magma overflow. Occurrence of the Pliocene age is the main composition of the Erta Ale volcanos in Ethiopian plateaus that bounds the northern MER. This indicates that subsidence of this region was gradual, and that it attained its present physiography with steep escarpments only in the Plio-Pleistocene (Chernet et al. 1998).

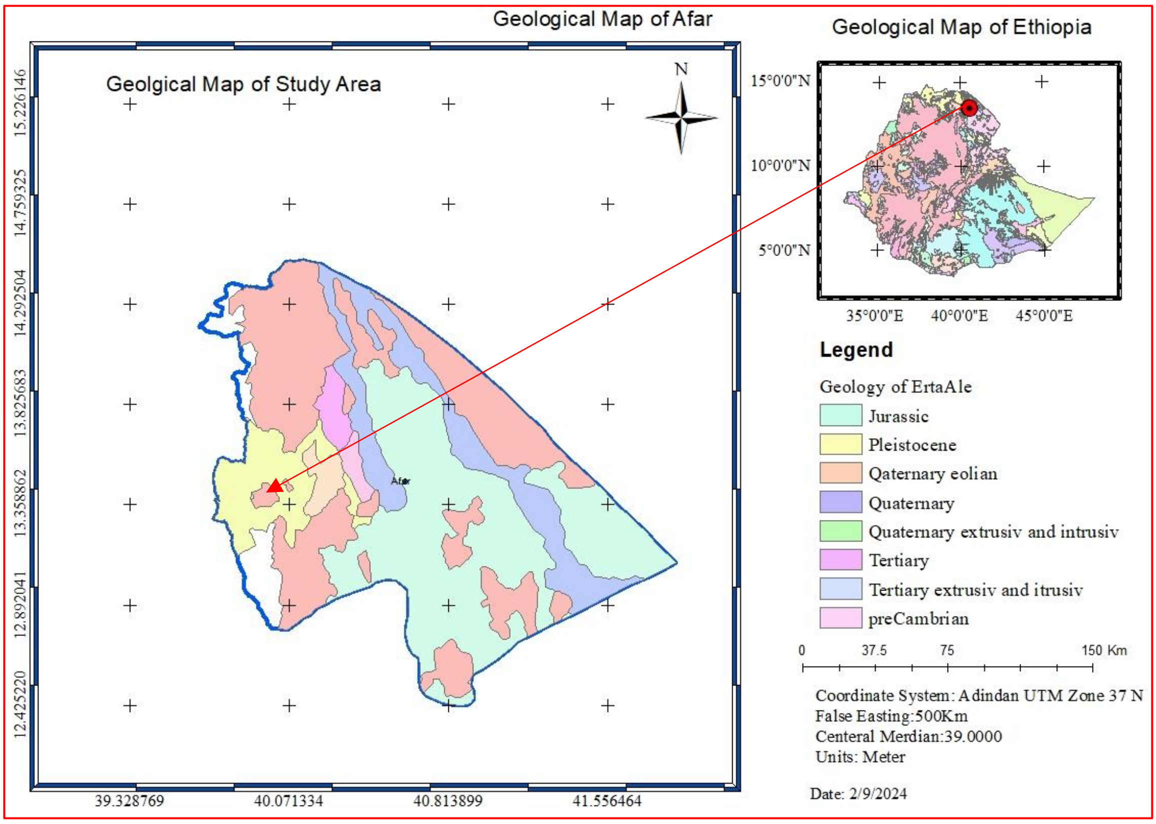

Figure 2. 1 Geological Map of Afar

Geology of Afar can grouped into four main types. These are Neoproterozoic basement, Mesozoic sedimentary rocks, Eocene–Miocene basalts, Miocene igneous rocks, Pliocene volcanic rocks; and Quaternary volcanic and sedimentary rocks (Varet 2018). Among those four types of geological units of Afar Pliocene and quaternary volcanic rocks are major components in Erta Ale and its surrounding areas. Quaternary volcanic rocks in the Afar Depression including the Erta Ale are composed of basaltic flows during refitting, scoria cones, and silicic rocks. This is tone of the main composition of the geology of the Erta Ale volcano.

As the figure 2.1 map show the geology Afar special the zone that Erta Ale. The map is crated from the geological map from the Ethiopian map sever website and Afar region is clipped with its geological data from the Ethiopian geology. The map found freely at https://www.ethiogis-mapserver.org/.

2.1.2 Afar Triple Junction and Tectonic Setting

The main causes for eruptive processes is the tectonic setting, that will determines how magma is generated and the pathways by which it reaches the Earth's surface. It also indicates the characteristics of eruptions (Xu 2020). The main Ethiopian refit system is approximately in northeast trending sector of the EAR system and it includes a series of rift segments extending from the Afar Triple Junction at the Red Sea-Gulf of Aden intersection to the Kenya Rift (Bonini et al. 2005). As the study of the (Hagos, Koeberl, and van Wyk de Vries 2016) indicates northern Afar Depression is one of the most volcano-tectonically active parts of the EAR system.

The formation this depression is associated with two large-scale processes. These are rotation of the Arabian plate concerning with Nubian/African plate and the emplacement of a thermal mantle account and normally beneath the continental lithosphere (F. Zwaan et al. 2020). The tectonic setting of the Afar is ~120 km long East African volcano system EAVS. It forms a part of the RSR branch of the Afar triple junction, that provides the separation three divergent plates (Lemenkova 2022; Moore et al. 2019; Xu 2020). These three divergent boundaries have their junction or meeting point at the Afar of active volcano of which is the main indicator of their crustal plate deformation. This place is place where the coastlines and plateau margins cannot neatly back into their pre-divergent entity. This is because the major constructive process of basalt generation has been a little excessive at this place and has created a new and youthful lowland that is the Afar (cited as Migoń, 2010). Study this tectonic activity is important issue that needs several studies in different disciplines. Because the final stage of the continental breakup hypothesis is the result of abundant magmatism.

Erta Ale is also one of the main volcanos that found at a place where oceanic rifting may be beginning to form an incipient oceanic crust. The triangular area covers an area of ~200,000 km^2 and is bounded by marginal escarpments, which are close to narrow axial zones (Beyene and Abdelsalam 2005). The location of Erta Ale is in northern end of the main MER. This place is meeting point for three velocity tectonic boundaries that are African, Somalian plate and Arabian including the Red sea these plates met at Erta Ale volcano north of Afar. The northern Afar including the study area Erta Ale is a well-defined asymmetrical depression adjoined on the west by the Nubian Plate and on the east by the Danakil Block (Doubre et al. 2017; Gudmundsson 2020; Hagos et al. 2016; Hamling et al. 2014). In the MER the active continental rifting creates landslide 16 formation, provides a prospective area to study the influence of tectonics (Martínek et al. 2021).

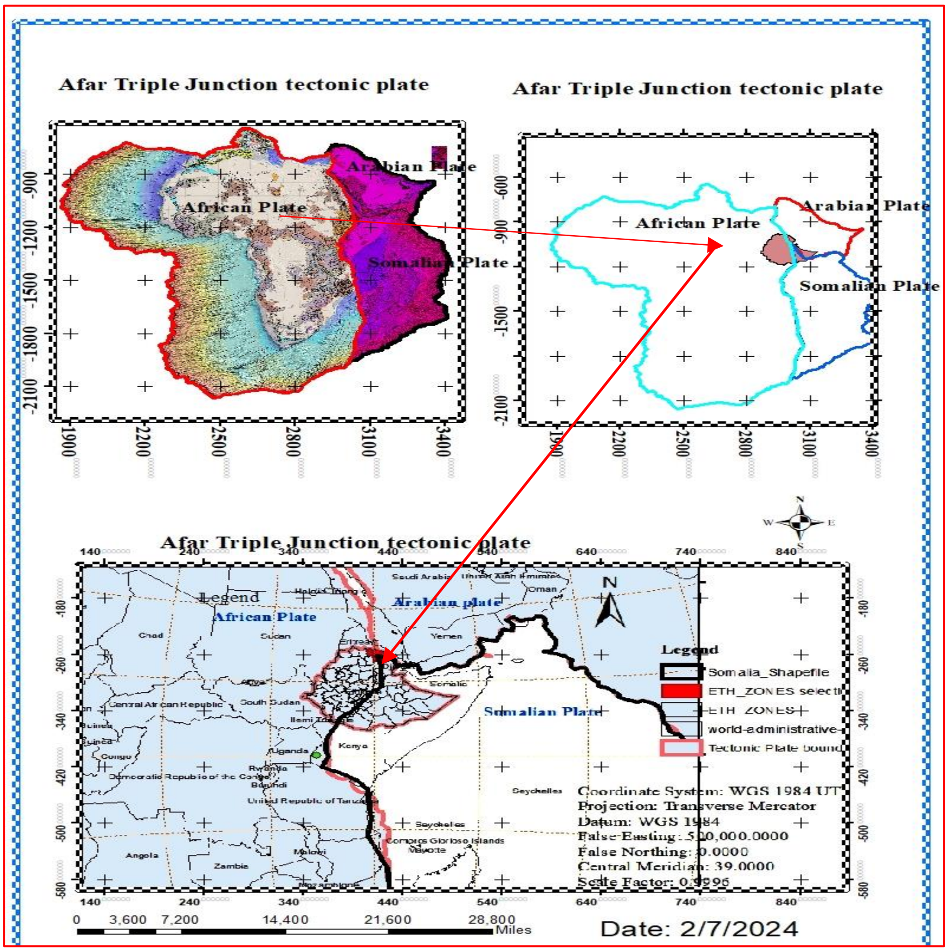

Figure 2. 2Tectonic Setting of Afar Triple Junction

As above 2.2 map shows, Erta 'Ale the tectonic setting of this active volcanos that is located at triple junction and an incipient mid-ocean ridge (Moore et al. 2019). The map created from Goggle earth world map, Ethiopian Boundary shape file, and world tectonic map from the goggle earth map and by digitizing this world plate tectonic map to three-plate divergent plates that meet at northern afar including active volcanos.

2.1.3 Ground Deformation Around Erta Ale Volcano

The shield volcano Erta 'Ale is situated in the Danakil Depression, Ethiopia, and is known for its active lava lake Erta Ale volcano has erupted since 1967 (before or after affter180 days) and it is an ongoing eruptive volcano (Barberi & Varet, .1970.). Its location is in the main MERS and erupted in November 2010, placing new lava flows on the main crater floor, the first such eruption from the southern pit into the main crater since 1973 (Field et al. 2012). The Erta Ale range is elliptical, with axes of 95 and 42 km, built by the activity of a series of NNW open fissures, running parallel to its main axe and there are six principal volcanic centres in the range. From north to south, Gada Ale, Aluo , Dala Fila, Borale Ale, Erta Ale, Hayli Gub, and Ale Bagu, the latter being the only one not located on the main axis of the chain. These volcanoes are all at a stage of fumarolic activity, some of them quite strong indeed, except Erta Ale in the craters of which molten lava lakes are usually present (Barberi and Varet n.d.; Ferretti, Prati, and Rocca 2001). The Erta 'Ale Lava Lake is found at Erta 'Ale axis of volcanic extension that 80 km long by 30 km wide (Barnie, Oppenheimer, and Pagli 2016). It has an open vent system that has continuous active lava lake at its summit that is responded dynamical pressure change in the magma reservoir at depth and these was overflowed lava to southern pit crater (Xu, Rivalta, and Li 2017).

Surface deformation in active volcanic areas indicates the movement of magma or hydrothermal fluids at depth and most researchers agree the active volcano is the result of the internal thermal pressurized molten magma (Pritchard and Simons 2002). Erta Ale was erupted in last three decade since 1970; However, the most recent volcanic activity began when the lava lake within its northern caldera overflowed on 16 January 2017 (Xu 2020). Studying active volcanoes' deformation at the local level is one way of monitoring the continental refit this is because the lava overflowing to the surface is the result of regional crust motion and the Red Sea crust. Because the lava that is spreading to the surface of the ground deformation will occurred, it is necessary to follow up the spreading rate as well as coverage of the deformation area per year. Because there is a neighboring place some km away from where people live, due to its fluctuation, it is necessary to check the lava lake level. Most of the study was intends to describe regional refit deformation. Studying volcanic eruption locally is better than regionally or crustal deformation studies to determine the local surface deformation and its effect on neighborhood places and people who live near the volcano.

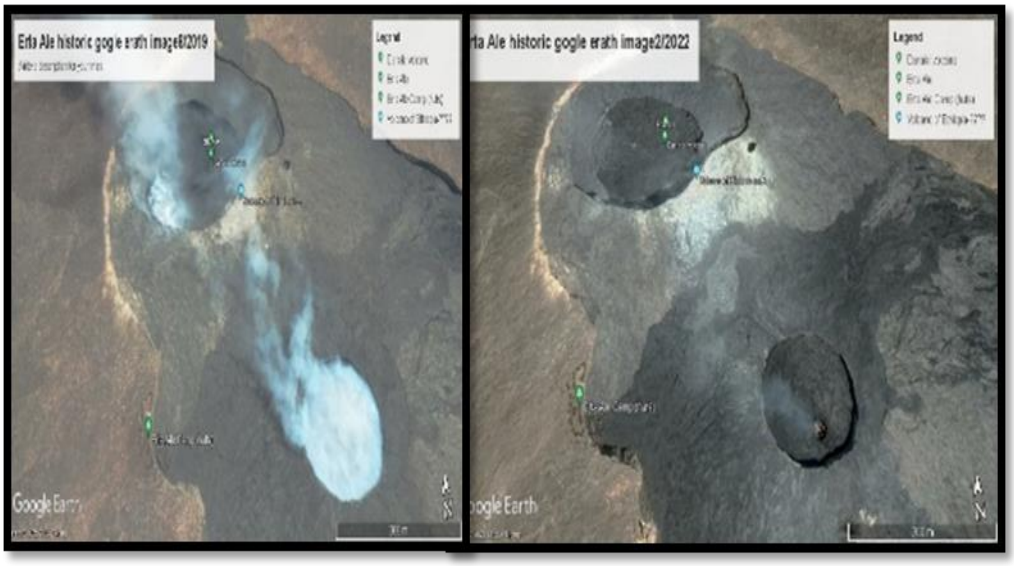

Figure 2. 3 Historical Image of Erta Ale

The above figure 2.3 shows there is higher thermal activity in 8/2019 than in 2/2022; this indicates there are still thermal fluctuations. (Xu 2020) describes the geometrical behavior and physical properties of the magma plumbing system beneath the two lava pits. The velocity of displacement observed after a volcanic eruption is dependent on the magmatic processes occurring at depth (Hamling et al. 2014). Monitoring the surface deformation has great significance, in exploring the activity and geophysical features of the underground deep pressure source in the volcanic regions. Size and shape changes of the magma chamber manifest on the surface in the form of terrain displacements, mainly by lifting in case of inflation and subsiding when the reservoir is deflating.

Different articles and journals describe the 2017 Erta Ale eruption and deformation trend. The study of ground motions associated with the January 2017 volcanic fissure eruption, and long term deformation pattern at Erta 'Ale in the time of building to following the initial eruption (Moore et al. 2019). (Xu 2020) shows that fresh lava flowed out and deposited on the flank of the volcano until late January 2020 without noticeable seismicity. As the (Xu, 2020) study shows maximum horizontal and vertical displacements from 2017 to 2019 is ~6 and 9 cm are observed near the northern pits that they are mainly caused by the contraction of a shallow dike. The volcanic activity is more at the time of eruption and it becomes smaller in magnitude. The velocity of refitting is also decrease when compared the start of the eruption (Xu 2020). Among those volcanoes of the Afar-Danakil Rift in northern Ethiopia, where the spreading rate is ~16 mm/year in the N77°E direction, have also been recently active (Xu 2020). As (Moore et al. 2019) study shows in the buildup eruption, from October 2014 to January 2017, they observed that gradual extension across the ridge axis at a rate of 60 ± 10 mm/year, over 3 times higher than the long-term plate spreading rate at Erta 'Ale.

2.2 Historical Development of SAR Technology

SAR is an advanced radar system that utilizes image-processing techniques to synthesize a large virtual antenna. This provides much higher spatial resolution than is practical using a real-aperture radar (Kim 2013). In 1953 Carl A. Wiley for the first time published basic principles of radar with Synthetic Aperture Radar (SAR) as a patent of specification with the title "pulsed Doppler Radar and means". SAR is an active imaging method by using microwaves that are used on mobile space vehicles either satellites or airplanes (Processing of SAR Data Synthetic Aperture Radar. II Series., n.d.).

American Carl Wiley first had the idea in 1951 of using platform movement and signal coherence to reconstruct a large antenna by calculation (Guanabara et al. n.d.). From synthesizing a large antenna aperture point of view, the SAR is based on the hypothesis that a target remains stationary during the data collection time interval while the radar antenna moves from one position to the next large antenna aperture (Soumekh n.d.; Victor C. Che and Marco Martorella n.d.).

In 1993, Goldstein presented the first satellite-based InSAR map showing large strains of the Earth's solid surface in this case, the deforming surface was an ice stream in Antarctica (Goldstein_RadioSci1988,n.d.). Sentinel SAR system transmits a long range of electromagnetic waves at a wavelength that ranges from a few millimetres to tens of centimetres and is unaffected by weather or clouds and can operate effectively during day and night under most weather conditions (Kim 2013). RADAR can mount on aircraft or satellites, and it can provide range sensitivity while avoiding ambiguous reflection. The first SLR was incoherence, which meant the phase information of the emitted as well as received waveforms could not retained and the physical long antenna that is real aperture the resolution is obtained in flight direction radar RAR. Because of restriction of antennal length in flight direction results in very coarse resolution that degrades the flight altitude by decreasing the area captured by satellite (Anon 2002; Monti-Guarnieri, Rocca, and Tebaldini 2018).

2.2.1 Types of SAR Observation

SAR can divided based on the satellite observation method as along-track and across-track interferometry. SAR operates at microwave frequencies and provides unique images representing the electrical and geometric properties of a surface in nearly all weather conditions (Simons & Rosen, 2015).

A. Along and Across Track Interferometry

SAR image from along track interferometry are obtained from different orbital positions or at different times but from the same position of the place. Along-track interferometry also called single-pass interferometry. Across-track interferometry is predestined for ATI, which compares the phase of two complex SAR images observed in the same geometries but separated by a short time span of data acquisition time (Krieger et al. 2010). This technique is useful for monitoring dynamic processes on the Earth's surface. Across-track interferometry is also called Repeat-pass which is acquired at different times and from different orbital positions (Pepe and Calò 2017; Xia 2010a; Yamaguchi 2020). In repeat-pass interferometric mode, only one radar antenna operated, which has two tasks at the same time: transmitter and receiver. This becomes an important technique to measure volcanic deformation at a horizontal resolution of tens of meters with a vertical accuracy of centimeters to fraction of centemeter (Lu et al., 2000). The first step to overcome the limitations of repeat-pass interferometry was the SRTM. It used to acquire interferometric data in a space borne in single-pass configuration. Across-track interferometry measures the look angle θ as a second coordinate and thus allows us to recover the point's location in space (Xia 2010a). Several SAR images acquired for the same area are obtained through the repeat illuminations of the SAR at different positions and times (Albino et al. n.d.; Doubre et al. 2017).

$$\triangle \varphi = -\frac{2\pi}{\lambda} \times \triangle r \qquad 2.1$$

Where Δ_{φ} is the phase change, r_0 is the slant range, $\boldsymbol{\theta}$ is the local incident angle and $\perp B$ is the baseline perpendicular to the line of sight. The following image is taken from (Krieger et al. 2010) and describes across-track interferometry.

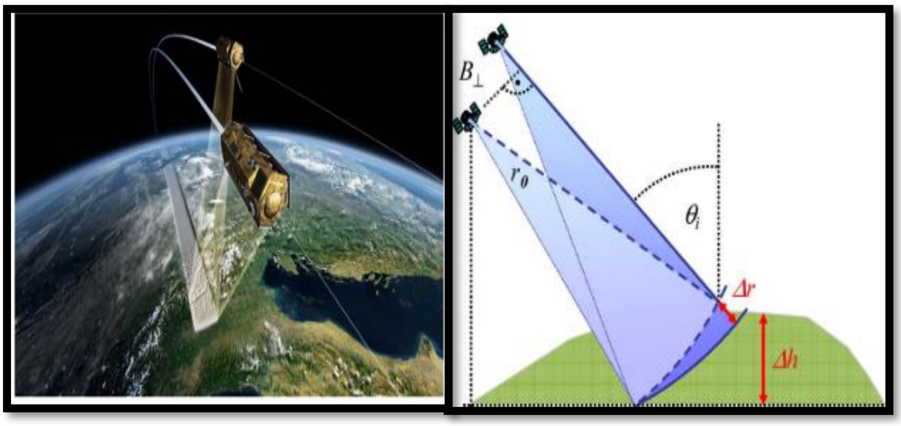

Figure 2. 4 Across track Interferometry

B. Amplitude and Intensity Interferometry

The signal resulting from the additive is not coherent; summing of the amplitudes for two incoming signals that results "amplitude" fringes or amplitude interferogram. In this interferometry, there are some problems because it is not possible to determine whether the interferometric signal is increasing or decreasing and it is not very accurate (Monti-Guarnieri et al. 2018). In multiplicative interferometry, it is possible to measure the interferometric phase by coherent cross-multiplication of the two input signals. In this type, the phase data indicate a better accuracy, as the fraction of the phase cycle is much easier to determine accurately.

2.3 SAR Data Processing Technique

A space geodetic technique is effective way to determine the ground surface displacement that occurred in time series. Permanent global positioning system GPS and SAR data in combines it is possible to detect deformation. However, permanent GPS sparsely distributed over world and the measurements are more applicable to detect crustal movement and the ground surface displacement by using the velocity field. It is more efficient for regional deformation than the local surface deformation. As the most current study shows, Global SAR measurements made over the past decades provide insights into the lateral extent of magmatic domains. SAR observes the change on surface of the earth overall world and they are useful to control volcano wide activities as well as it has great potential for monitoring topographic change detection. The distribution of eruptive activities and rifts that causes surface displacements can be studied using InSAR at subaerial volcanoes (Bagnardi and Hooper 2018) . There are different types of InSAR processing methods; DInSAR has been compared to the permanent scatters interferometry

(PS-InSAR); both have advantages and disadvantages and both methods are complementary (Oštir and Komac 2007).

2.3.1 In-SAR

InSAR is the initial SAR data processing technique from two sentinel images captured at different times or in different orbital orientations to determine the phase change between them. It uses the phase components, which are co-registered SAR images of the same area to estimate the topography and measure the surface change in the hazard area of earthquake and volcano. InSAR is a method in which two radar scenes acquired in the same area at different times could provide radar phase information (Lemenkova 2022; Marghany 2020; Younis 2020). It is a technique that two radar scenes observed in the same area but at different times can generate radar phase information (Wang et al. 2019). InSAR uses the phase components of co-registered SAR images of the same area to estimate the topography and measure the surface change in the hazard area of earthquakes and volcanos (Kim, 2013). The term SAR interferometry is for all methods that employ at least two complex-values SLC images to get more information about the object than present in a single SAR image by exploiting the phase of the SAR signals and second SAR image to provide additional information in at least one imaging parameter, must be different compared with the first image. It is the multiplication of a single look complex (SLC) data in the first date and a complex conjugate of SLC data in the other acquisition date that generates an interferogram which contains topographic, atmospheric effect, baseline error, multi-temporal and noise components (Kim 2013). While SLCs usually come with radiometric calibration factors already applied, speckle noise remains unmitigated in these full-resolution products.

It gives more information about the object than is present in a single SAR image by exploiting the phase of the SAR signals (Xia 2010b, 2010a). InSAR become an essential technique which is used to process SAR data to detect ground surface deformation and its rate due to volcanoes, earthquakes, landslides, glaciers, and aquifers (Rongier et al. 2019). However, its limitation is its inability to remove the residuals from the incoming phase intensity. It shows only the fringe or interferometry from only two images. However, the time series deformation could not be determined. It is a method that two radar scenes acquired in the same area at different times could provide radar phase information (Wang et al. 2019). This type of SAR data pro3cessing technique used in previous initial time and the only possibility is generating the interferogram from two SAR images. It combines two complex SAR images to form both the complex interferogram and the coherence map that provides fundamental analyses of the exploitability of SAR interferogram. At each position, a pulse is transmitted, and the return echoes pass through the receiver and are recorded in an 'echo store (Chan and Koo 2008). The figure above shows the interferogram from the two SAR images of Erta Ale. This fringe shows abundant noises and a composite of different phases such as, the flat earth effect, topographic phase effect, and atmospheric phase effects.

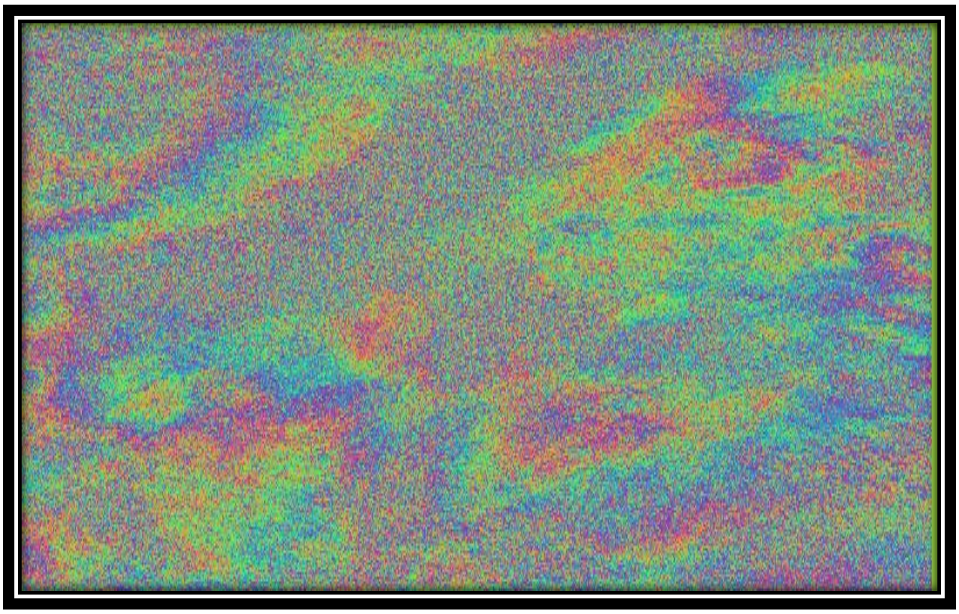

Figure 2. 5 Fringe in InSAR

The above figure indicates the interferogram generated from the two SAR images.

$$\triangle \varphi = -\frac{4\pi}{\lambda} \times \frac{b_{\perp}}{rsin} + \frac{4\pi}{\lambda} d_{LOS} \qquad 2.2$$

Radiometry represents ground reflectivity to microwave: Phase is the sum of two terms:

$$\triangle \varphi = \varphi_{\text{specific}} + \varphi_{\text{D}} \qquad 2.3$$

The phase term accounts for the interaction between wave and land, which is called the specific pixel phase and is noted by $\varphi_{\text{specific}}$ is connected to the physical nature of the land and the look angle. The phase term that accounts for the round trip propagation; each time the wave crosses a distance equal to wavelength λ, its phase increases with (Guanabara et al. n.d.):

$$2\pi : \varphi_D = \frac{4\pi}{\lambda} \qquad 2.4$$

The distance D is conventionally representation of the range from the source to the centre of the pixel.

$$\delta\varphi = \varphi_2 - \varphi_1 = \frac{4\pi}{\lambda}(D_2| - |D_1|) \qquad 2.5$$

Both SAR images are composed of a regular grid with complex values, or phasors, which can be decomposed in an amplitude and a phase component.

$$y_1 = A_{b\times} e^{-j\phi_b} e^{-j\frac{4\pi}{\lambda} r1} \qquad y_2 = A_{b\times} e^{-j\phi_{b\times}} e^{-j\frac{4\pi}{\lambda}(r2+r1)}$$

$$\psi_1 = ^{-j\frac{4\pi}{\lambda}\times(r2+r1)} \qquad \psi_2 = ^{-j\frac{4\pi}{\lambda}\times(r2+r1)}$$

Where A_1 and A_2 are amplitude. *2. 6*

2.3.2 D-InSAR

D-InSAR phase measurements are wrapped between -***π*** and +***π***. SAR interferometry nowadays is mostly used for the detection and monitoring of surface changes. It is an effective method for mapping of land, ice, and even the sea surface topography occurring during passages of the RADAR sensor over the same scene (Guanabara et al. n.d.; Pepe and Calò 2017). It used for different applications during the last time. It can detect change in different areas including urban and the displacements of surface over large temporal and spatial scales with precision in the cm and even mm range (Xia 2010b). It is a toll to determine and monitor the surface displacement due to volcanos, earthquake, and any man made changes on to the earth. However, it has key limitations, atmospheric error on the interferograms cannot removed and this errors are called decorrelation phenomena (Lanari et al. 2007). D-InSAR is techniques that calculates the phase difference and produce the interferogram fringe for two SAR images that captured in separated observations time of an investigated area. It provides a measurement of the ground deformation projection along the radar LOS (Lanari et al. 2007). Interferometry uses phase data SAR images that is very sensitive means of distance measurement, or more exactly of distance variations because it makes sense only in a differential manner. Finite analysis of phase differences between two radar images makes it possible to reconstitute landforms or to measure land movements that may have taken place between several data collections with millimetric precision (Guanabara et al. n.d.). The differential InSAR method has its limitations such as changes in the reflection of target objects or areas, atmospheric influences, and signal disturbances (Oštir and Komac 2007). D-InSAR has a deficiency in removing all the noise in DEM; its key limitations are due to the noise effects on the interferograms, referred to as decorrelation phenomena which can be said that these noise phenomena are the consequence of any effect leading to differences in the radar observation (Xu 2020). As most study describes for analytical purposes, D-InSAR method uses coherent radar targets that can be clearly distinguished in all images and do not vary in their properties (Chen and Zebker 2002; Oštir and Komac 2007; Puglisi and Coltelli 2001). The interferogram is derived through an exact co-registration of images and a complex multiplication of pixel values from the first image with the conjugated pixel values of the second image (Oštir and Komac 2007). D-InSAR used to create accurate digital elevation models and small surface displacements. Its ability is generating DEM that shows the topographic nature of the earth surface. The phase difference between the two-interferogram images can calculated as:

$$\phi = \phi_1 - \phi_2 = \frac{2\pi\rho}{\lambda}\delta \qquad \varphi_{12} = \frac{\lambda}{4\pi} \times \delta R_{2} - \frac{\lambda}{4\pi}\delta R_1 \qquad 2.7$$

$$\delta = \frac{\lambda\phi}{\lambda\rho} \qquad 2.8$$

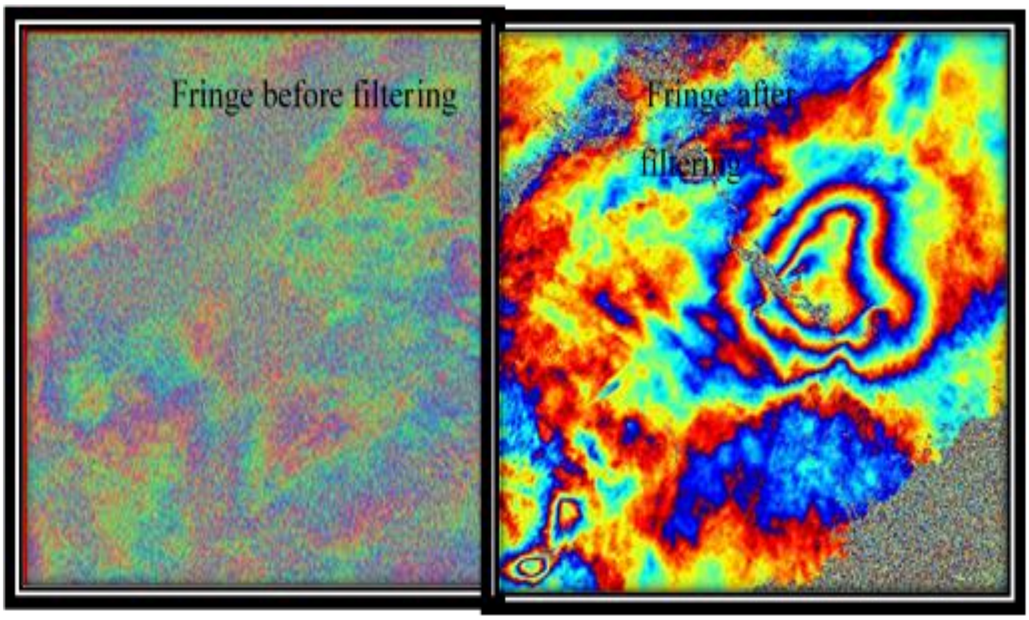

Figure 2. 6 Interferogram after error removal

Figure 2.6 indicates the interferogram generated between two SAR image before filtering and After filter or InSAR and D-InSAR. D-InSAR interferogram shows more clear number of fringes with color sequence and it will show DEM.

2.3.3 PS-InSAR

PSI is a powerful remote sensing technique able to measure and monitor displacements of the Earth's surface over time (Crosetto et al. 2016). D-InSAR do not represent continuous deformation graph or map for time series displacement.

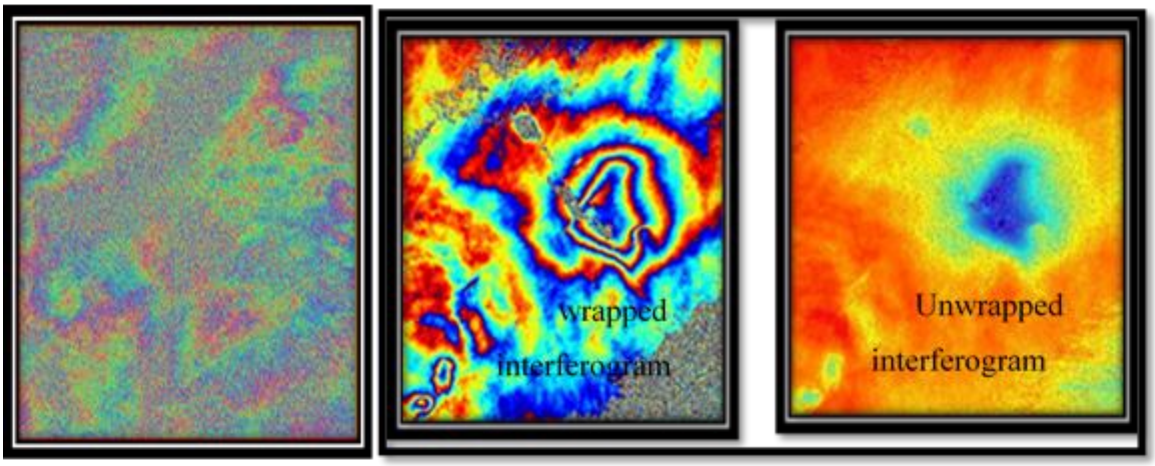

Figure 2. 7 Wrapped and Unwrapped interferogram

The above figure shows the unwrapped interferogram generated from S-1A SLC data vertical polarization from slave February 2017 and master image January 2020 at Erta Ale volcano. It shows the difference between the three SAR processing techniques. Wrapped interferogram can only represent from minus pi to pi. The unwrapping phase is final interferogram that shows continuous deformation.

PS-InSAR is an upgrade of D-InSAR; for analytical purposes, this method uses coherent radar targets that can be clearly distinguished in all images and do not vary in their properties (Chen and Zebker 2002; Oštir and Komac 2007; Puglisi and Coltelli 2001). This method shows continuous deformation graph for time series displacement. It is an advanced method of SAR data processing that developed by Politecnico of Milano. It also has the main limits of conventional approaches to surface deformation detection because of temporal and geometric decorrelation.

This needs the further correction of geometry of the pixel and temporal decorrelation. Some of this are remove during co-registration process. It is an operational tool to determine ground deformation in millimetric level and high spatial density grid of phase stable radar targets the so-called PS acting as a "natural" geodetic network. This geodetic network created in triangulation network and to this thesis, The data are a set of points with a density depending on the form and coverage of the surface.

$$\phi_{int} = \phi_{flat} + \phi_{topo} + \phi_{defo} + \phi_{atmo} + \phi_{noise} \qquad 2.9$$

The reflected signal ϕ is a superposition of several components can attribute to different phenomena with contributions due curvature of earth ϕ_{flat} satellite angle of observation. ϕ_{defo} , the ups and downs of earth or real topography ϕ_{topo}; ϕ_{defo} surface deformation/displacement ϕ_{atmo} atmospheric delay; ϕ_{tempo} temporal decorrelations due to rockslides, sediment transport, and vegetation changes; and ϕnoise remaining perturbations due to thermal and orbital errors (Redadda, Boualleg, and Hamdi 2009; Rongier et al. 2019; Wang et al. 2019). The interferogram is processed using SARPROZ software using PSI method from multiple image interferogram generation. The unwrapped interferogram shows the deformation phase after all residual phase errors removed from the total incoming phase. Phase unwrapping errors severely affect the estimation of earthquake and volcano source parameters using interferometric observations. Therefore, it is desirable to avoid phase unwrapping completely (Jiang and González 2020). The interferometric phase can calculated as the difference between the measured (unwrapped) phase ϕ and the expected phase for the reference body ϑ derived from the orbit geometry, hence

$$\partial\phi = \phi - \vartheta \qquad 2.10$$

The influence of topography and surface displacement D_p the interferometric phase differences relative to the reference body can calculated as follows.

$$\partial\phi_p = -\frac{4\pi}{\lambda} \times (D_p - \frac{B_{\perp p}^0}{R_{1p} sin\theta_p^0} H_p) \qquad 2.11$$

Since the measured interferometric phase is the sum of the reference phase ϑ and the deviations:

$$\phi_p = \partial\phi_p + \partial\vartheta_p \qquad 2.12$$

Where the reference phase is determined by:

$$\vartheta_p = \frac{4\pi}{\lambda} \times Bsin(\theta_p - \alpha) \qquad 2.13$$

We can find

$$\phi_p = \frac{4\pi}{\lambda} \times (Bsin(\theta_p - \alpha) - D_p - \frac{B_{\perp p}^0}{R_1 sin\theta^0} H_p) \qquad 2.14$$

2.4 InSAR Error Budget For Deformation

The total phase data for incoming interferometric phase obtained from the satellite is composed of intensity and amplitude. This is also composition topography, and deformation, with the Atmospheric phase, flattening phase, and other noise coming together. The use of SAR interferometry is often impeded by decorrelation from thermal noise, temporal change, and baseline geometry (Goldstein and Werner 1998). The main problem this is how to display such phase data separately and it needs some process to separate them. In addition to this, some errors affect the final output analysis. In order to remove such effects different mechanisms and algorithms are used. There are several some errors like, atmospheric, temporal, multi path and other noises may observed in interferogram. Phase unwrapping errors severely affect the estimation of earthquake and volcano source parameters using interferometric observations (Jiang and González 2020).

2.4.1 Topographical Phase

Topographical, DEM and Flattening phase are not error. However to determine the deformation phase for the ground surface they are reduced. Topographical phases are not the actual error; however, to determine ground deformation we reduce it as residual from interferogram. Unwrapped, co-registered interferogram include topography, atmosphere and deformation signals (Osmanoğlu et al. 2016). The high resolution external EDM (SRTM30) used for primary geocoding that removes topographic phase values. SRTM digital elevation model was used to remove the topographic phase (Samsonov et al. 2008).

$$\varphi_{flat} = \frac{4\pi}{\lambda B||} \qquad 2.15$$

Where the B || is the parallel baseline for each pixels from the reference master image in interferogram. The topographic phase is the phase component of the interferogram related to the topography above the reference ellipsoid and is proportional to the perpendicular baseline (Osmanoğlu et al. 2016).

$$\varphi_{topo} = \frac{4\pi}{\lambda B_{\perp} R .sin\, \theta.\Delta z} \qquad 2.16$$

Where φ_{topo} is the topographic phase contribution, $\perp$B perpendicular baseline, R is the range between the satellites, target **θ** is the look angle and △z is the topography above the ellipsoid.

2.4.2 Orbital Error

To reduce the orbital error all images must be set with an external orbit. To remove orbital error all images to must set to external orbits. Modern SAR satellites have small orbital tube and by downloading images with short revisit time, we can reduce orbital error. In addition to this setting all images to external orbit is the main mechanism to remove the errors due to satellite orbit. The most popular method used in orbital-error correction is surface fitting with linear or quadratic models, using unwrapped phase observations (Tian et al. 2018). To reduce orbital error the base line distance of all images must be as short as possible. In this study area, most data baseline distance is between ~-100 and 100. Without knowledge of the baseline, an exact calculation of the height is not possible (RI 2019). The normal baseline Bn is the distance between the master and the slave's track, measured normal to the slant range, azimuth plane. The contribution of the target P to the phase of the interferogram would be proportional to the travel path difference between the two acquisitions 4p (Achmad and Lee, 2021; Externe, and Interne 2013; Fornaro et al. 2006; Goldstein and Werner 1998; Lanari et al. 2007).

$$phase = \Delta\frac{4\pi}{\lambda} \times \left(R_s(p) - R_M(p)\right) \qquad 2.17$$

Where R_S and R_M are respectively the slave-target and the master-target travel path, and p is the transmitted wavelength. VV polarization allows having two polarizations of the same wavelength at high temporal integrity (Braun and Offermann 2022).

2.4.3 Atmospheric Error

Signals pass the atmosphere twice; and there is water vapour or moisture, dust particles, pressure and temperature troposphere layer and different ions in ionosphere layers that increase or decrease the time of signals to reach the target and back to the sensor. Temporal and geometrical decorrelation affects SAR interferometry and limits its operational activities for surface deformation monitoring and topographic profile reconstruction. Moreover, atmospheric phase error can strongly decrease the accuracy of the results (Ferretti et al. 2001). The influence of the atmosphere on the radar interferometric phase is mainly caused by temporal and spatial variations in the atmospheric refractivity (Cong et al. 2018). Removing the atmospheric phase effect in the final deformation is necessary because it affects the final displacement value. Atmospheric phase screening is done to remove the tropospheric and ionosphere signal errors like water vapour density, temperature, and pressure of the troposphere layer water vapor density, temperature, and pressure of the troposphere layer (Data and Izumi 2023; Khalili et al. 2023). Several Nr models are used to determine APS; homogeneous (isotropic) Nr distribution which shows a linear relationship concerning position in the range may be valid for areas of soft topography. The other one inhomogeneity of Nr as a linear trend concerning the range which is a linearly varying Nr model and applicable to the topographic area without elevation assuming multicollinearity between the slant range distance and the elevation variables. Another model which applies to this study is the empirical polynomial model which takes into account the inhomogeneity of the APS in both the range and azimuth directions (Data and Izumi 2023; Izumi et al. 2021). The third model is the empirical polynomial model and takes into account the inhomogeneity of the APS in both the range and azimuth directions these methods are supplemented by additional filtering to remove the APS from the time series, by firstly high-pass filtering in time, then low-pass filtering in space to calculate the APS, which is then removed from the time series (Moore et al. 2020). The widely used phase filtering methods can be grouped into three categories: spatial domain, transform domain, and nonlocal NL methods, single-scale (Pu et al. 2020). The APS can be computed by using known atmospheric models and can be removed from observations or estimated by InSAR temporal and spatial data (Khalili et al. 2023). Most of the PSC are identified after APS estimation and removal using a time series analysis of their phase values (Ferretti et al. 2001).

$$\varphi(t) = \frac{2\pi f \int n(r,t) dr}{c} \qquad 2.18$$

Where n is the atmospheric refractive index, r is the position, f is the carrier frequency, c is the speed of light and t is the moment of the signal transmission n can be calculated as;

$$n_{r=1+10^{-6}N_r} \qquad 2.19$$

For radio frequency, N_r can be defined as (Kim 2013).

$$N_r = \frac{77.6P}{T} + \frac{10^{-5}}{T^2} e \qquad 2.20$$

The direct wave phase is used as a reference for cancellation during the synchronization processing. The part interferometric phase that is affected by the atmosphere can be modelled as:

$$\Delta\varphi atm(t_m, t_s, x, y) = \Delta\varphi atm(t_m, t_s, x, y) - \Delta\varphi atm(t_m, t_s, 0,0)$$

$$\frac{2\pi f}{c}[n(t_m) - n(t_s)]\Delta r \qquad 2.71$$

Where $\Delta r = R_{SP} + R_{AP} - R_{SAT}$ The residual atmospheric phase error can be expressed as follows.

$$\Delta\varphi atm(t_m, t_s, x, y) = \frac{2\pi f}{c}\Delta n \Delta r \qquad 2.22$$

Where Δn is an error of the atmospheric refractive index. Another error that affects the surface over the period between observations(Zebker and Villasenor 1992). The value of temporal coherence is one which implies there is no a change at the surface.

2.5 Data Processing steps in PSI

In the pursuit of extracting time-series deformation information from SAR data, PSI stands out as the most effective method to process and analyze the time span deformation. PSI is particularly adept at mitigating atmospheric effects in interferograms by leveraging multiple InSAR pairs over extended periods, facilitating the identification and suppression of atmospheric phase influences (Kim 2013). Its efficcacy in removing atmospheric phase residuals makes PSI the preferred tool for data processing in this study. The ensuing sections expound upon the method employed for data processing, analysis, and presentation of results using various tools. Overall steps of the research are categorized into the following main steps.

2.5.1 Set the Orbit

Upon downloading the SLC SAR image, the initial step involves importing the data into SARPROZ software. The precise orbit is then set to ensure accurate processing. Identification of the master image, which serves as the reference for all slave images, follows. The SAR image's file type used to determine surface deformation is the single look complex, containing crucial phase information. This phase information is utilized to estimate topography and measure surface changes in earthquake and volcano hazard areas. After setting the orbit, an AOI can be selected to optimize disk space utilization and processing time.

2.5.2 Master and Slave Extraction

After the software sets the precise external orbit of the all images, master image can be selected with small perpendicular baseline distance relative to slave. It also has high coherence valve usually 1 and low atmospheric and temporal errors. All slave images are extraction has done. After the software arranges the slave with time series order, that is ready to coregister to reference image. A master image is chosen from the available SAR images based on geometry related to all other images, high coherence, and possibly lowest atmospheric disturbances modelling item data (Gehlot et al. 2005). The normal baseline Bn is the distance between the master and the slave’s track, measured normal to the slant range, azimuth plane (Fornaro et al. 2006). The following graph connection represents all interferograms generated concerning one single image. The following graph shows all 26 images of slave neighborhoods base line distance that use master image reference to process the rest of the application.

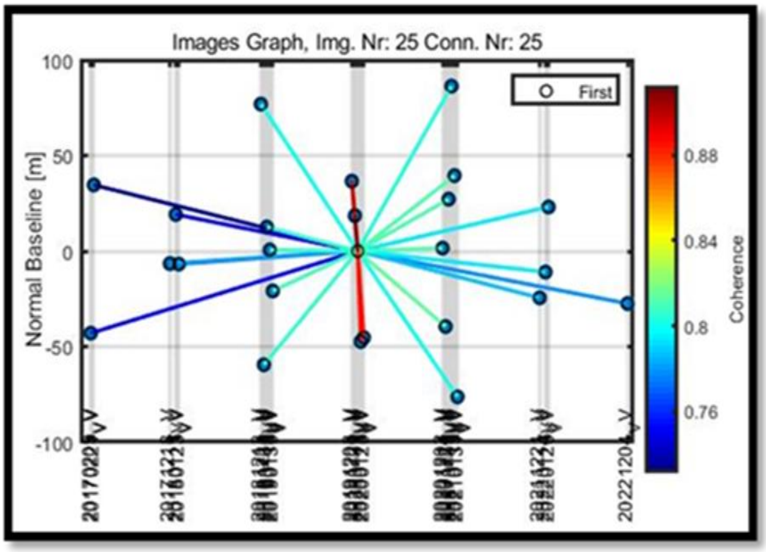

Figure 3. 1 base line distance

The above figure indicates the relationship of all slave with master image in perperdicular baseline distance.

PS-InSAR time series processing is multi-image processing in the case of SARPROZ software, which needs a minimum of 20 images. In this study, the software by default selects an image captured on July 16/2020 with a baseline distance of 0m and the highest coherence of one as shown below. The baseline distance for all slave image is between ~100m and ~100m that is good range to reduce errors.

2.5.3 Image Co-registration

SAR image co-registration is the first and main technique before starting InSAR time-series analysis. We select orbit as the initial offset parameter that amplitude cross-correlation method, with reference windows 64×64; pixel search 12×12; correlation windows 64, Win 16; threshold correlation 0.3, threshold nosing 1.5 max roots mean square RMS 0.05, minimum point 50 and the spectral diversity phase filtering. Multi-image co-registration is the key procedure before starting time-series analysis (Pepe and Calò 2017). Using large estimation windows (i.e., averaging the data over large areas), many stable targets surrounded by non-coherent clutter are lost. Similar considerations hold for the coherence threshold (Grandin et al. 2010). To be co-registered slave SAR images must be TOPS split and changed in the same orbital system. It is the aligning of

SAR images from two antennas and those determine accurate phase differences as well as reduce noise. It allows the determination of a geometric transformation that may exist between two image signals (Yu et al., 2007). Image co-registration is used to align all slave images to the master images corresponding to the same scene acquired at different times, with different sensors, or under different conditions (Li et al. 2022). It improves the accuracy of the ground surface deformation in the whole process (Yu et al. 2007). Amplitude cross-correlation is the primary input parameter data that would be used to support the co-registration step (Hatton 2020). SAR co-registration is done in three main steps; these are an estimation of offsets between several tie patches with amplitude cross-correlation, fitting of a polynomial wrap function to a set of tie-patch offsets, and resampling of slave image (Wang, Jónsson, and Hanssen 2012). The Goldstein phase filter was applied to the clarity by removing noise and used to increase quality of interferograms by making the interferometric fringes visually clear (Mancini, Grassi, and Cenni 2021; Tzouvaras, Danezis, and Hadjimitsis 2020). Spatial and temporal de-correlation effects were roughly reduced by the master image during co-registration.

2.5.4 Amplitude Stability Index

Amplitude stability index is generated from co-registered SAR images as PS has the characteristic of the stable backscatter in images collected at different times, the phase stability is often considered as a criterion for selecting PSs (Jia and Liu 2016). The reflectivity map created from the amplitude of the SAR time series data of those slave and master co-registered images geocoded in Goggle earth map. Once amplitude stability index specified the GCP points generated that used as the reference point to process the rest of SAR processing. The following map is reflectivity map before geocoding and after primary geocoding. This increases the quality of result that processed later steps. It shows the limit of the study area and it is possible to reduce or increase the study areas, as we need. This map is the reference data for all APS data processing step. Figure 3.2 indicates the coregisterd images after primary geocoding, it is more aligned to the exact position to real ground. Creating the reflectivity map amplitude stability index provides both topographic and back-scattering features of the terrain that allow to carry out of classification and morphological analysis on the same data set avoiding errors introduced by a bad co-registration between different data sources (Bamler 2000; Puglisi and Coltelli 2001). The phase stability can be assessed according to the signal-to-clutter ratio (SCR) The average SCR of a pixel is more than a given threshold, the pixel can be regarded as a

PSC point(Ferretti et al. 2001). For this project, we select 0.85 threshold to select 1532 stable points that makes 4571 connections.

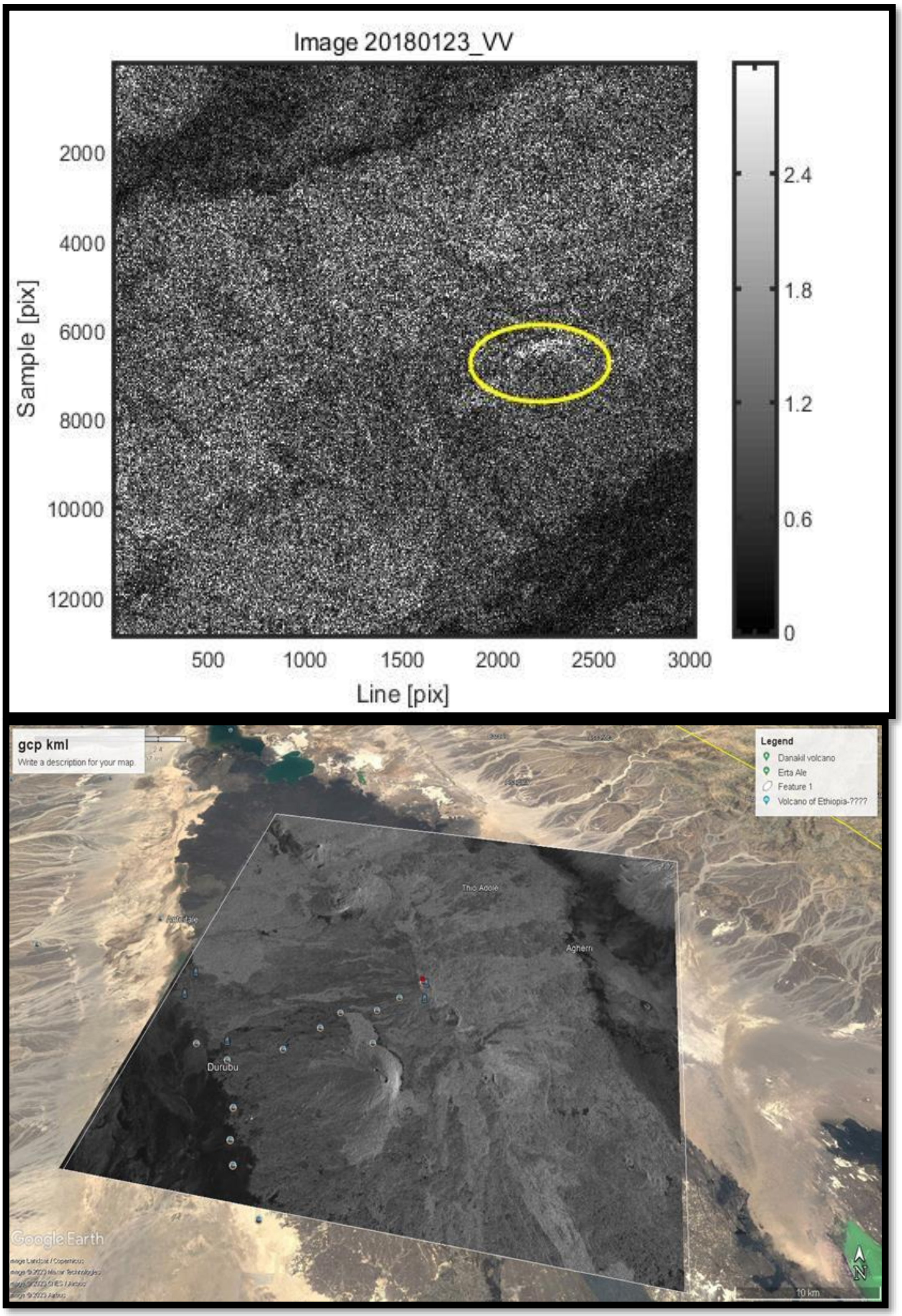

Figure 3. 2 Co-register map after primary geocoding

The above figure indicates the phase image is more accurate and clear overlapped to its real ground after preliminay geocoding. This will decrease the geometrical decoloration for the final interferogram.

2.5.5 DEM Generation

The automatic DEM was packaged or linked in SARPROZ during data processing and this used to NASA, SRTM 30m DEM data were used for removing the topographic phase from interferogram (Habte 2021; Staniewicz et al. 2020; Suwarsono et al. 2020). The DEM generated from selected GCP, northing 1504033.0m, easting 679581m, and universal traverse Mercator UTM zone 37. All images are in the northern hemisphere with ellipsoidal world GIs (WGIS84):545 and samples ID 6443, line1514 by using a grid of 3.69m, in-ground range as well as 14.00 in-ground azimuth. The need for differential range measurements accurate to millimeter to achieve required elevation accuracies leads to the use of phase instead of time delay in radar interferometry and is the reason that InSAR is a coherent SAR.

Residuals related to topography can be cancelled using an external DEM (Mora, Arbiol, and Palà 2006). The orbital parameters of the SAR acquisitions, consider no height errors on the DEM. The nominal range R formed from phase of SAR image pixel can expressed as:

$$\phi = \phi_G + \phi_\rho = \phi_G + \phi_\rho \pm -4\pi\left(\frac{R}{\lambda}\right) \qquad 2.23$$

R is the slant range to the pixel at the centre of the synthetic aperture and φ_G : is the phase shift due to the complex gain of the radar receiver and the image formation processor. φ_ρ is the total phase of the composite reflectivity of the scatters contributing to the pixel.

$$\Phi_r = -4\pi R/\lambda \qquad 2.24$$

This is the deterministic phase shift due to the two-way path length to the pixel centre. The quantity φ ab is called the IPD, which is a very sensitive indicator of range differences and thus depression angle and elevation (Melvin and Scheer 2013). From the following DEM, the four points encircled with an ellipse show the extent of the study area. This is an area with a radius of 20km from the center of the study area approximate center is the Erta Ale lava lake reservoir. This DEM is externa DEM generated from SRTM, however, there is some error; because it is more courser than SAR-generated DEM. The final Elevation DEM map shows all errors eliminated in APS.

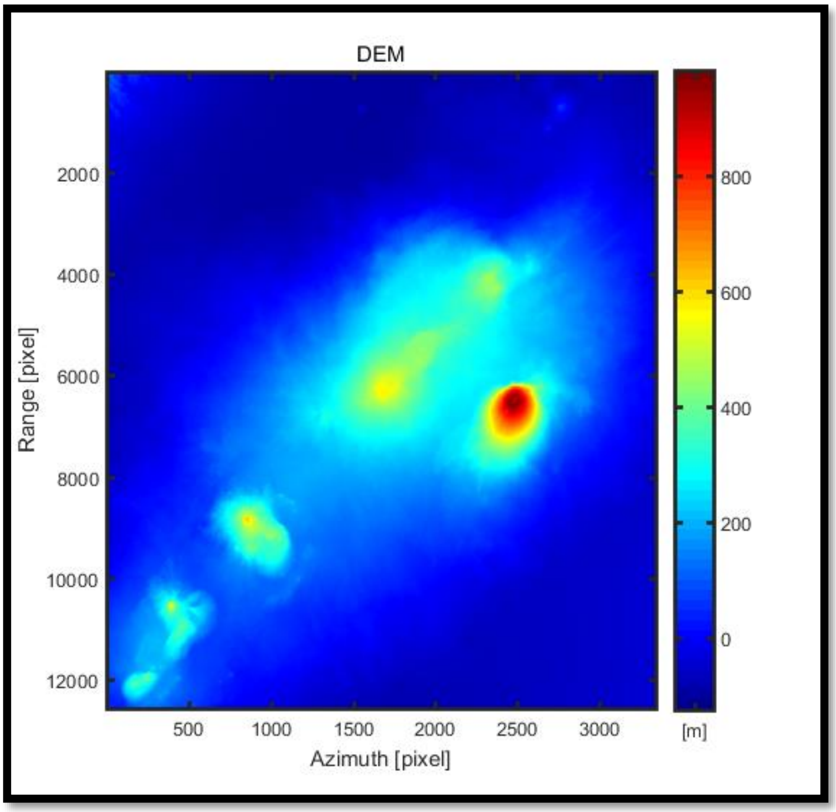

Figure 3. 3 DEM

The above DEM is generated from the SAR coordinate and used to generate the height displacement value during deformation analysis. This DEM is more clear than SRTM and more accurate because it is generated from densed PSC.

2.5.6 Creating a Coherence Map

To generate a coherence map we select the parameters; the primary parameter is the amplitude stability index reflectivity map generated from the coregistered SAR data. The amplitude of the complex correlation coefficient is called coherence (Zebker and Villasenor 1992). Coherence map is used to determine the characteristics of the study area change and it is used to determine elevation of the study area. The pixels with high amplitude values indicate better coherence and a smaller amplitude deviation index indicates better stability (Liu et al. 2022). After the coherence map, it is possible to estimate the inverted residual, such as atmospheric residuals and deformation.

The interferometric coherence map, generated by calculating the normalized inter-image correlation, characterizes the uncertainty with which the height can be measured (Redadda et al. 2009). To do this the first input is the reflective index map generated from the terrain backscatter and atmospheric stability scattered map after errors related to the atmosphere are eliminated. Thermal coherence is negligible due to the high signal-to-noise values of the target InSAR systems. Coherence is high when the two images are spatially matched to the same position and low when mismatched in their position. However, in this study, temporal and thermal coherence are neglected because of the small baseline between interferometric acquisition and a large scattering window.

InSAR phase coherence can be expressed by the aggregation of the following components (Redadda et al. 2009; Zebker and Villasenor 1992).

$$coh_{map} = coh_{temporal} \times coh_{spatial} \times coh_{thermal} \qquad 2.25$$

$$\gamma = \frac{|s_1 s_2{}^*|}{\sqrt{(s_1 s_1{}^*)(s_{,2} s_2{}^*)}} ,0 < \gamma < 1 \qquad 2.26$$

Where S1 and S2 are the complex data related to a pixel of each acquisition, |s1s2*| is the modulus operator, and denominator {} indicates the expectation value. The modulus of the complex coherence |γ| provides an estimation of the accuracy of the interferometric phase ϕ. In practice, under the assumption of ergodicity and considering locally stationary processes, the expectation operator can be replaced by spatial averaging to obtain the maximum (Iglesias et al. 2014).

2.5.7 Interferogram Generation

Upon generating the coherence map, the subsequent step involves creating an interferogram, illustrating the phase difference between master and slave images captured at distinct times or orientations. Preliminary steps include flattening and removing the DEM. A modified Goldstein filter is then applied to enhance interferogram clarity by eliminating noise. Employing multi-looking with a window size of 15×15 and a pixel size of 1×1 contributes to exploiting phase information from at least two complex-valued images, revealing additional object details compared to a single image (Xia 2010a).

The SARPROZ software is employed in this project for multi-image APS processing, generating an interferogram from one master image and all other slave images after co-registration. Each interference or fringe within the interferogram signifies a 2π change in the wave phase, often represented using a color scale (blue-green-yellow-red) or greyscale (Universitaria et al., 2002).

From interferogram we can display deformation about the area. This can be calculated by counting the fringe cycle by multiplying wav length. To identify the deformation type one must consider color sequence. Both SAR images consist of a regular grid with complex values, decomposable into amplitude and phase components. The reflected signal ϕ is a superposition of several components, which can be attributed to different phenomena with contributions due to ϕ_{noise} satellite angle of observation; ϕ_{flat} flat spheroidal shape of the Earth; ϕ_{topo} topography; ϕ_{defo} surface deformation; ϕ_{atmo} atmospheric delay; ϕ_{tempo} temporal decorrelations, for example, due to rockslides, sediment transport, and vegetation changes; and ϕnoise remaining perturbations, for example, due to thermal and orbital errors (Rongier et al. 2019; Wang et al. 2019).

$$\phi_{int} = \phi_{flat} + \phi_{topo} + \phi_{defo} + \phi_{atmo} + \phi_{noise} \qquad 2.27$$

Φ_{int}= total interferogram phase map captured by satellite from the target ground surface.

Φ_{flatt}=the phase contribution due to curvature of the earth.

Φ_{topt}=the phase value due to the topography of the ground surface.

Φ_{defo}=the phase value due to the displacement of the position of a point on the target.

Φ_{atmo}=the phase value due to the atmospheric effect.

Φ_{noise} phase effect due to temporal scatter and look angle.

The interferogram is obtained through a fine coregistration of images and once the interferogram is generated, the across-track interferometer contains a record of the variability of the height of the surface or phase of height. This can be done by inversio of phase to reconstruct the height (Borghero 2017; Hamling et al. 2014; Lu et al. 2000; Nobile n.d.; Yu et al. 2007). The total range difference between the two observation points that the phase represents can be many multiples of the radar wavelength or, expressed in terms of phase, many multiples of 2pi. A process of typical approach to get a unique phase that is directly proportional to the range difference is to first determine the relative phase between pixels called phase-unwrapping which can adjusted by an overall constant multiple of 2pi (Simons and Rosen 2015).

2.5.8 Phase Unwrapping

A straightforward approach to phase unwrapping involves deriving the first differences of the phase at each image point along one dimension, utilizing an approximate derivative, and subsequently integrating the results. Direct application of this approach may lead to the propagation of local errors due to phase noise. When multiple interferograms with various baselines are available, they can be compared to enhance accuracy (Simons and Rosen 2015). The integration of the differenced phase about any closed path yields a value equal to the sum of the enclosed points of variability. In all cases, there will be individual pixels or areas incorrectly assigned to multiples of 2π, and identifying these points without additional information can be challenging. The unwrapped phase is derived from the slant range and the wavelength (λ) of the radar signal (Monti-Guarnieri et al. 2018). The unwrapped phase ϕh can be obtained by unwrapping the ideal interferometric phase φc after removing the flat-earth phase, and their relationship can be expressed as the

$$\varphi c = angle\theta \ (exp(j\phi h)) \qquad 2.28$$

where angle returns the phase angle. The real interferometric phase typically contains noise, and the presence of noise increases the difficulty of phase unwrapping, reducing its accuracy, which directly impacts the accuracy of the obtained height h. Therefore, interferometric phase filtering is a critical step before unwrapping.

$$\varphi_N = \int_{m=0}^{N} \varphi'_m dm \ ; \quad \varphi_0 = 0 \qquad 2.29$$

where φ_0 is the reference point. φ_N is the endpoint, m is the integration variable(samples along the measurement axis) and φ_n' is the complex phase derivative

2.5. 9 APS Estimation

The atmospheric phase term in a single-look complex (SLC) image is defined by the refractivity index Nerf(rs, t), a spatiotemporal function of temperature, pressure, and partial pressure of water vapor (Iglesias et al. 2014).

A. Sparse Point Selection

Under these processing steps, crucial steps are undertaken. Initially, processing parameters are selected, with a focus on the Amplitude Stability Index. Taking this as input, the first step involves selecting sparse points with a high coherence threshold of 0.85. A seed pixel is chosen as the starting point of a region, and adjacent non-region pixels are successively added if they can be reached without crossing phase gradients falling below a certain threshold (Chen and Zebker 2002). The amplitude threshold is applied for selecting Persistent Scatterer (PS) points and pixels with high amplitude values..

B. Delunary Graph Creation

Following PS selection, first-order Persistent Scatterer Candidates (PSCs) form a reference network for the entire target area (Jia and Liu 2016). From the selected PS points, a triangulated Delaunay graph is created. Delaunay triangulation ensures that the minimum angle of the triangles in the triangulation is the maximum among all possible triangulations of the graph (Lee and Lin 1986). The phase height coefficient in the spatial domain can be calculated from this Delaunay triangulated network graph.

Let S be any set of N points in the plane and let DT(S) be the graph of the Delaunay triangulation of S. For all points a and b of S, let d(a, b) be the Euclidean distance from a to b and let DT(a, b) be the length of the shortest path in DT(S) from a to (Dobkin, Friedman, and Supowit 1987).

There is a constant independent of S and N such that

$$c \leq \frac{1+\sqrt{5}}{2}\pi \sim 5.085, (\frac{DT(a,b)}{d(a,b)}, c) \qquad 3.8$$

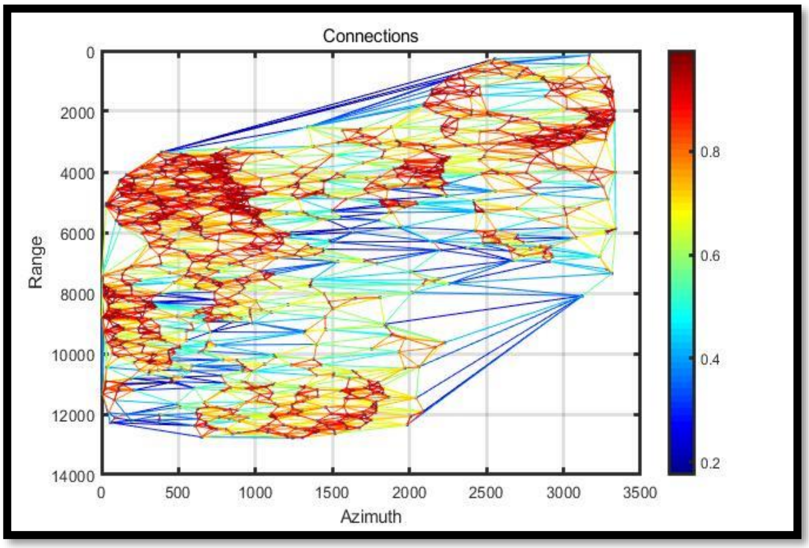

Figure 3.5 Delunary graph connection from PSC

The above triangulated network is created from different PSC.

C. Determining the Inverted Residuals

Errors such as flat earth, temporal, and multi-path are addressed during the earlier interferogram generation stage. Phase filtering is crucial in interferometric synthetic aperture radar (InSAR) applications, including deformation monitoring and topographic mapping (Pu et al. 2020). The key factor in Persistent Scatterer InSAR (PSI) is the deformation model for phase modeling and parameter estimation, often utilizing a linear model (Jia and Liu 2016). Non-local (NL) techniques efficiently reduce noise while preserving structures through weighted averaging of similar pixels (Deledalle et al., 2011). PS-InSAR provides determination of atmospheric phase residuals, and the topographic phase is removed using the external DEM SRTM30. In this area, there may be many dust particles from the loose clay. Atmospheric phase residuals, determined by the Atmospheric Phase Scattering method in SARPROZ, are affected by high temperatures at active volcanoes.

The accuracy of surface displacements measured by differential radar interferometry is significantly degraded by APS (Izumi et al. 2021). Changes in atmospheric conditions, particularly pressure and water vapor, between two SAR acquisitions induce phase delays in an interferogram that can potentially obscure real ground deformation signals (Albino et al. 2022). The atmospheric effect on time series deformation contributes to cumulative displacement.

2.5.10 Final Result Geocoding

Potential inaccuracies in orbit parameters and reference point selection may lead to misalignment of geocoded results on the reference grid (Gehlot et al. 2005). Geocoding of the interferogram is performed at SRTM30m resolution to mitigate topographic phase effects resulting from the moving body effect. However, given the global nature of SRTM, the final displacement images must undergo geocoding terrain correction (Beal 1979; Fornaro et al. 2006; Melvin and Scheer 2013; Pepe and Calò 2017; Suwarsono et al. 2020; Xia 2010a). The geocoded results are further referenced to Google Earth for alignment with surface features, facilitating cross-checking within the designated study area. This alignment serves as critical evidence to support the formulation of conclusions.

2.5.11 Time Series- InSAR Report Preparation.

The final time-series results are documented in SARPROZ under the time series module, marking the conclusive phase of data processing using the software. In-depth deformation analysis is conducted within the time series framework, complemented by supplementary analyses employing ArcGIS, Google Earth, and MATLAB. Post-atmospheric phase removal from the time series displacement, outputs are saved and exported in various formats, including maps, graphs, diagrams, and CSV files. The CSV data undergoes further processing to articulate the results in numerical form and generate additional hypotheses. All findings from this study are comprehensively discussed and presented in detail in the subsequent chapter.

Chapter Three

3.Method and Material

3.1 Description of the Study Area

The focus of this study is the Smoking Mountain Erta Ale volcano in Afar, Ethiopia, which serves as both a research and tourist destination. Researchers from around the world have conducted studies in this area at various times. Beyond its significance as a research site, Erta Ale is also a geotourism center in the Afar region. Positioned near Dalol, the lowest point below sea level, its geographical coordinates range from 13° 20'N to 13° 50'N latitudes and 40°30'E to 41°00'E longitudes (Habte 2021). The site is approximately 550 km north of Addis Ababa and is part of tourist corridors, owing to its captivating natural features and its central location for visiting other northern Ethiopian tourism sites.

Erta Ale, characterized by a basaltic shield, exhibits crack formations and fountain temperatures of 1175°C, as compared to previous pyrometer measurements of 1165°C Situated in the remotest and lowest elevation on Earth, Erta Ale boasts a unique land formation within the Great Rift Valley system. Despite being an unstable region, it attracts researchers and tourists alike due to its extreme conditions, with an average temperature of 50 degrees Celsius and a strikingly colorful landscape. Its location is in transit corridor for northern Ethiopian tourist center. It is very amazing place especially at night one can enjoy the magma molten or Firing Mountain.

The location of Erta Ale, near the lowest elevated point of Dallol, contributes to its warmer weather. The northern Afar region, also known as the Danakil Depression, gradually narrows to the Gulf of Zula (Beyene and Abdelsalam 2005). The climate in the study area lacks vegetal soil, providing an ideal condition for exposure, and geological contacts are visible both in the field and on aerial photographs (Barberi and Varet n.d.). Erta Ale is situated on an incipient mid-ocean ridge and has demonstrated ongoing activity until at least June 2019, as indicated by (Doubre et al. 2017; Lemenkova 2022).

The following figure 3.1 indicates the geographical location of the study area. It shows spatial position in Ethiopian regional map and the specific geographical extent of Erta Ale in final geocoded goggle earth map. This chapter serves as the pivotal section of the study, delineating the data sources, processing methodologies, and analytical approaches utilized to assess deformation in the Lava Lake pits of the Erta Ale volcano.

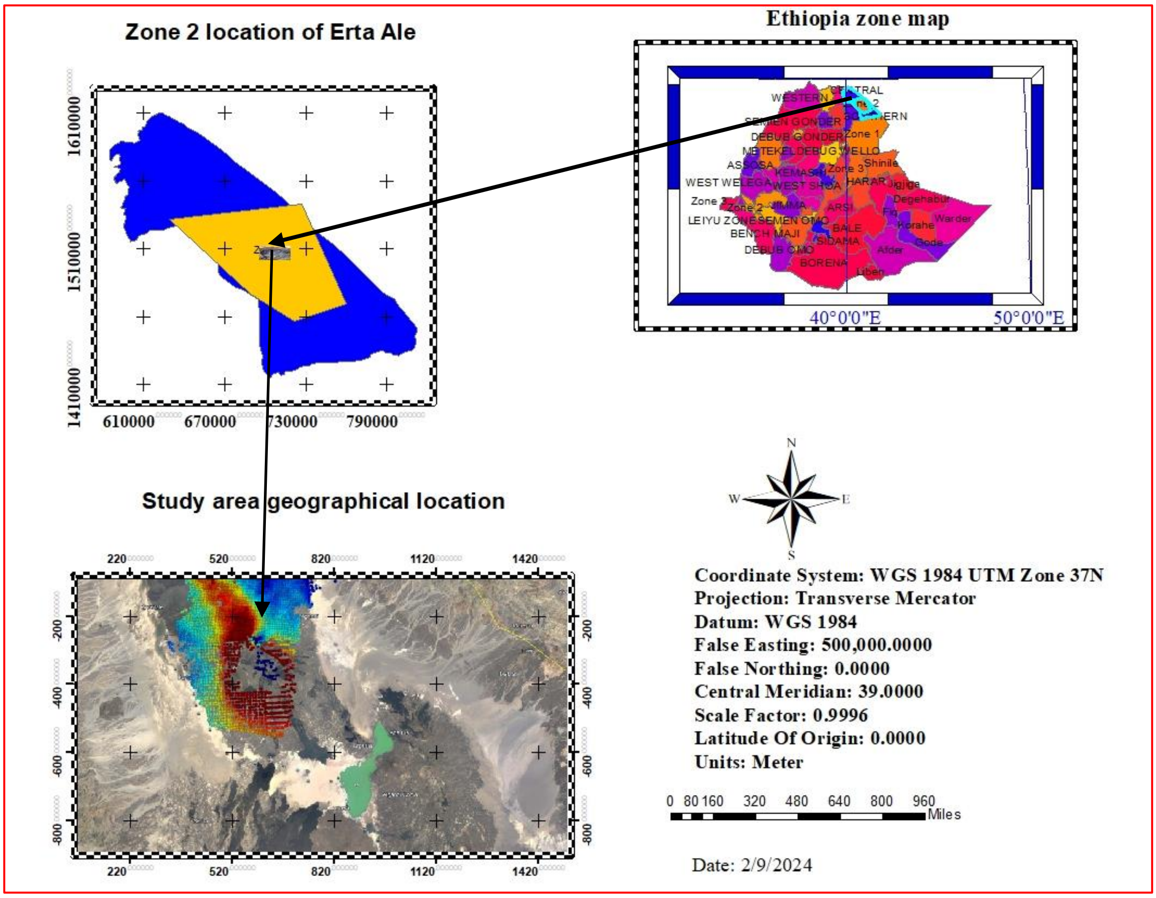

Figure 3. 4 geographical location of study area

The above map shows the geographical location of the study area from the Ethiopia the zone 2 is the location of Erta Ale volcano in Afar region.

3.2 Materials Used For Research

The essential materials for this study encompass software, computer resources, and the SAR data that is input crucial for result analysis. Sentinel-1A SLC SAR data in the descending direction, spanning from January 2017 to December 2022, serves as the primary input. SARPROZ software, augmented by additional tools like MATLAB, ArcGIS, Google Earth, Microsoft Visio, and QGIS, is employed for both processing and post-processing stages. A licensed version of the commercial SARPROZ software facilitates the processing and analysis of time-series SAR data.

3.2.1 Data Set

The primary data employed for this study comprises space geodetic SAR data. PSI, an advanced SAR interferometry technique, is chosen for its capability to mitigate atmospheric phase errors in the final displacement results. The SARPROZ software, specifically designed for SAR data processing, is instrumental in implementing APS corrections. The SAR space geodetic data, obtained as open-source satellite data, is accessible through the Alaska Satellite Facility ASF website at https://asf.alaska.edu/ or the European Space Agency (ESA) open hub. Downloading time-series SAR data for surface deformation determination entails specifying the study area's spatial location and adhering to criteria outlined in Table 3.1. 25 Sentinel-1A data acquisitions, spanning from February 2017 to December 2022, were downloaded, surpassing the minimum requirement of 20 SAR images for time-series deformation analysis.

Table 3. 1 Sentinel - 1A parameters

No	Parameter	Item Description	No	Parameter	Item Description
1	Data set	Sentinel	6	Wavelength	5.6
2	Sub Set	S-1A	7	Frame	548
3	Satellite flight direction	Descending	8	Path	79
3	Acquisition mode	IW	9	Band type	C- band
4	Polarization	VV	10	Images	25
5	Product Type	SLC	11	Acquisition period	Jan 2017 to Dec 2022

The selection criteria for downloading Sentinel-1 data from the ESA/Copernicus open hub are depicted in Table 3.1. The descending direction is favored for this study due to its comprehensive coverage over the study period and superior accessibility. With a revisit time of six days or three times per month, the orbital error is minimized, considering the dependency of satellite orbit on Earth's rotation. The Terrain Observation with Progressive Scans (TOPS) technique, involving long bursts and antenna rotation, is employed for co-registration and ground surface analysis.

3.3 Research Aproach

The research is conducted to study ground deformation at Erta Ale volcano in Afar Ethiopia using the PSI from February 2017 to December 2022. Ground surface deformation needs time series data. For this research the SAR data from the ASF website https://search.asf.alaska.edu/#/ is processed by latest and effective method for atmospheric phase error. The necessity of the research is most of the study are focused on the continental crustal deformation than local ground surface deformation. This needs the analysis of surface displacement at volcano. The final output of the research that answer the objective of the research is expressed in form of quantity. In this approach, the quantitative values are used to analyze the result. The final output of the study is represented in interns maps, table and graphs that represents numerical value of ground deformation. The research design is quantitative approach and the conceptual framework of the research is indicated by flowchart.

3.4 Conceptual framework of methodology

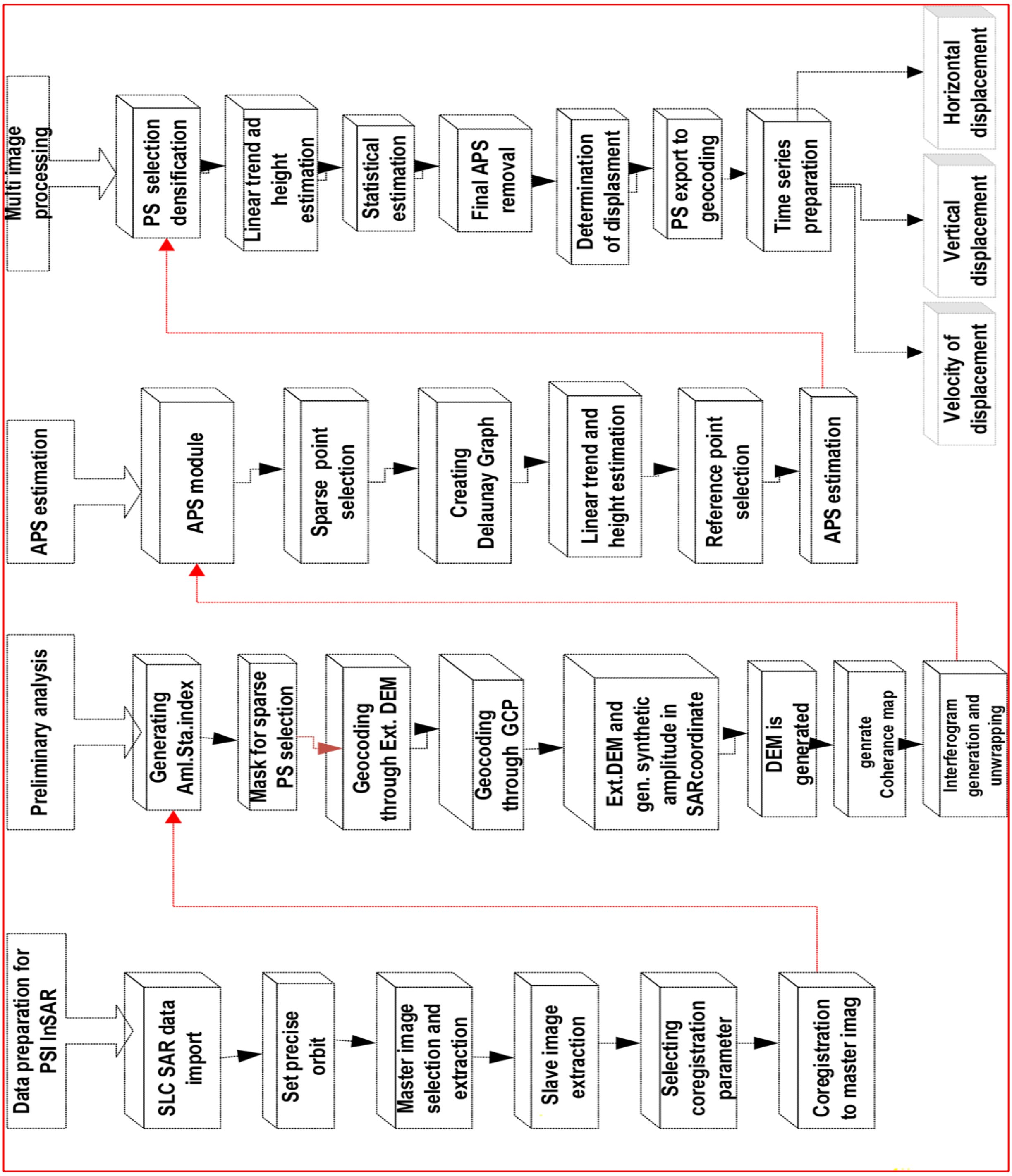

Figure 3. 5 Flow chart diagram for data processing

The conceptual framework, illustrated in Figure 3.1, focuses on the data processing stages, excluding the introduction, literature review, and final thesis report writing. The overarching processing steps for this thesis project fall into three main categories: preparation stages, preliminary stages, estimation, and multi-image PSI processing.

Chapter Four

4. Result And Discussion

4.1 Result

The study's conclusive outcomes are analysis of the ground surface deformation surrounding the Erta Ale volcano in northern Afar, Ethiopia. Producing 25 SAR interferograms from the Sentinel-1A descending images spanning February 2017 to December 2022, the study employs Interferometric Synthetic Aperture Radar (InSAR) to extract information about heights or displacements (Pu et al. 2020). PSInSAR emerges as a superior method for determining time-series deformation. That is its ability to remove the atmospheric phase error PSI is more effective to determine time series deformation.

The InSAR images, originating from the surface, amalgamate distinct signal phases from ground targets, the atmosphere, and various other influences. To derive deformation results, phase information is systematically reduced from the original image through processes such as spectral diversity, Goldstein phase filtering, and co-registration. These steps effectively mitigate earth curvature effects, flattening, using the external DEM and temporal variations, and other sources of noise.

4.1.1 Coherence Map and Interferogram

The coherence map serves as a crucial tool in elucidating the surface deformation pattern. The study area, encompassing a 20 km radius from the center of Erta Ale volcano, lacks water bodies and vegetation, minimizing additional speckle noise and ensuring higher coherence. The creation of 25 interferograms from co-registered master and slave images allows for a comprehensive analysis of ground surface displacement patterns and directions based on coherence values. The interferograms reveal a consistent and nearly uniform fringe in 2017 around active volcanoes, attributed to lava overflow in the vicinity. Interferometric Synthetic Aperture Radar (SAR) data yield reflectivity, interferometric phase, and coherence images (Deledalle et al. 2011). Coherence values, particularly efficient for visualizing time-series displacement, culminate in an unwrapped map after the removal of all residuals in the last third image. The steeped interferogram indicates high ground deformation and gentle fringe implies small ground change. The color sequence in interferogram can indicate the deformation pattern and types. From the color sequence red to purple is uplifting (inflation) and if purple to red indicates subsidence or deflation.

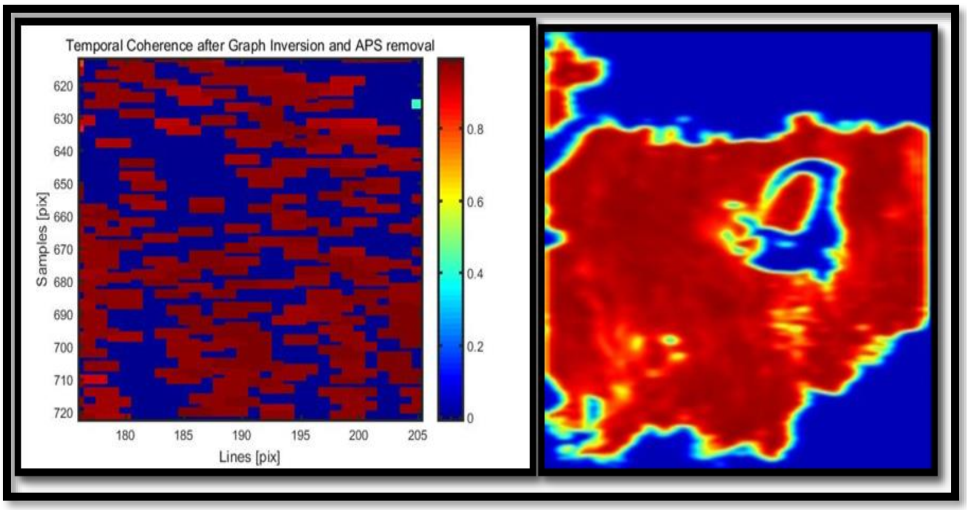

Figure 4. 1 Coherence map

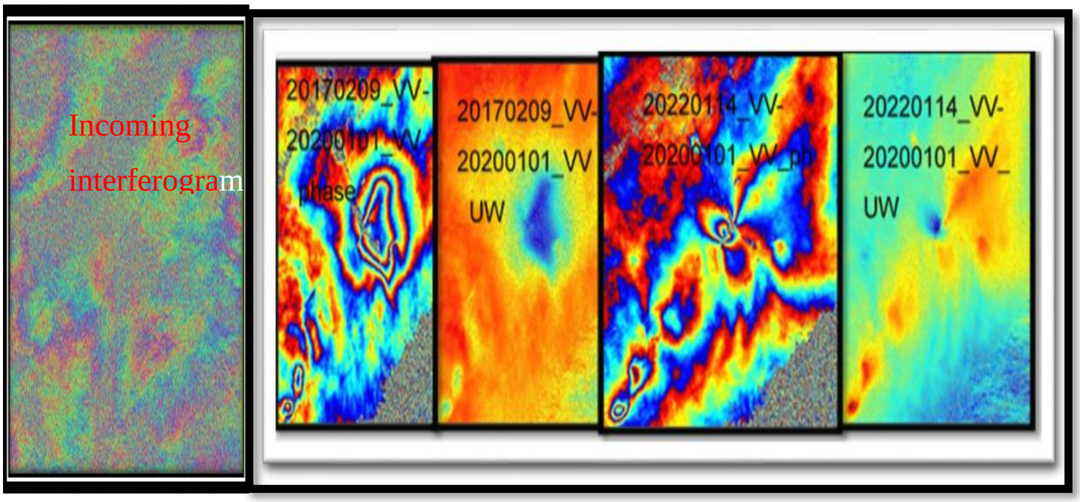

Figure 4. 2 Wrapped and Unwrapped interferogram

Figure 4.1 indicates the coherance map indicates the relationship from temporal and the atmospheric. Figure 4.2 indicates the procedure of the interferogram generation. For the two comparable times.

The interferogram and historical images exhibit analogous geometrical patterns, indicating congruent results between the two datasets. However, the interferogram alone provides a qualitative and quantitative understanding of deformation, relying on the observation and counting of fringe colors from the outer periphery towards the central region. The challenge lies in quantifying the deformed areas numerically based solely on the interferogram.

To address this limitation, additional analysis is conducted to calculate the total subsidence and uplifted areas. Utilizing Google Earth historical images from January 2017 and December 2022, the study employs the digitization of two boundary edges of the Lava Lake. Areal changes in the Lava Lake are determined by calculating the differences between the initial and final stages of the study period. The digitized Geographic Information System (GIS) map provides a visual representation of the extent to which the active volcano's Lava Lake area has diminished during the specified time interval.

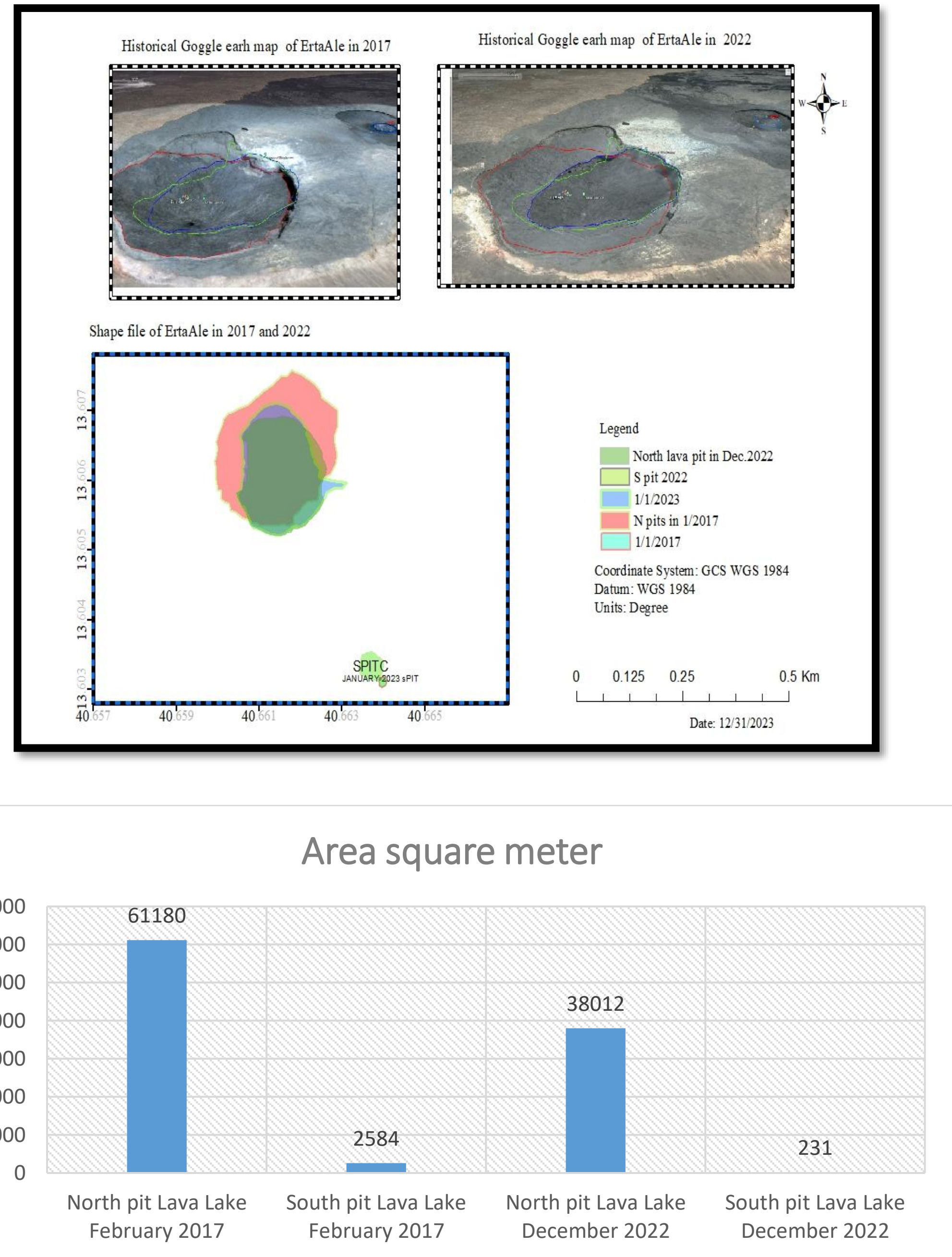

Figure 4. 3 The shape file of lava lake

The above figure shows the areal change of the magma at the two lava lake pits. This map is created from the goggle earth historical image.

4.1.2 Residual Displacement

Permanent deformation, as defined by (Tang et al. 2023); is a lasting alteration in ground surface caused by events such as volcanic eruptions. This study observes horizontal and vertical residual ground deformation from February 2017 to December 2022. This displacement shows the permanent displacement in last study area. Employing the APS method, atmospheric errors are remooved from the time series SAR data, facilitating the generation of residual deformation in both vertical and horizontal dimensions. The resultant map illustrates the permanent deformation at the conclusion of December 2022 for each stable point throughout the study period. Notably, this deformation is evident around active volcanoes, including Borale volcanoes and Erta Ale, where changes are attributed to magma overflow and crustal motion.

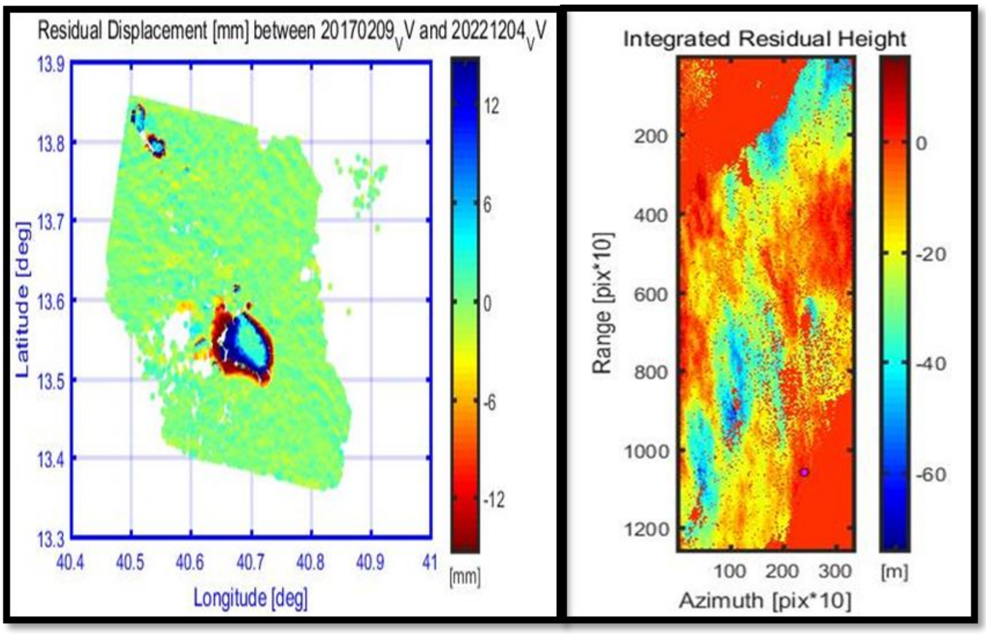

Figure 4. 4 Residual displacement

Figure 4.4 indicates the permanent deformation during the last six years caused by Erta Ale volcano. There is extension and contraction in horizontal displacement ad deflation and inflation of the vertical displacement.

4.1.3 Cumulative Displacement

Following the deduction of all phase values from the intensity and amplitude-phase SAR images, the final output show cases deformation from January 2017 to December 2022. The cumulative displacement, essential for understanding the ongoing deformation dependent on past displacements, represents the summation of linear displacement values annually from a specific time reference.

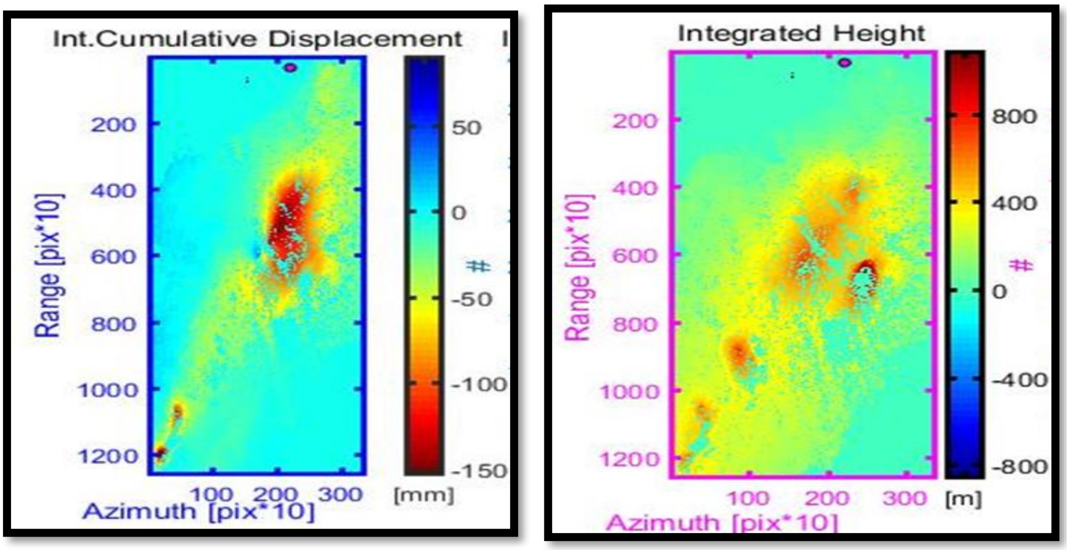

Figure 4. 5 Cumulative displacement and height

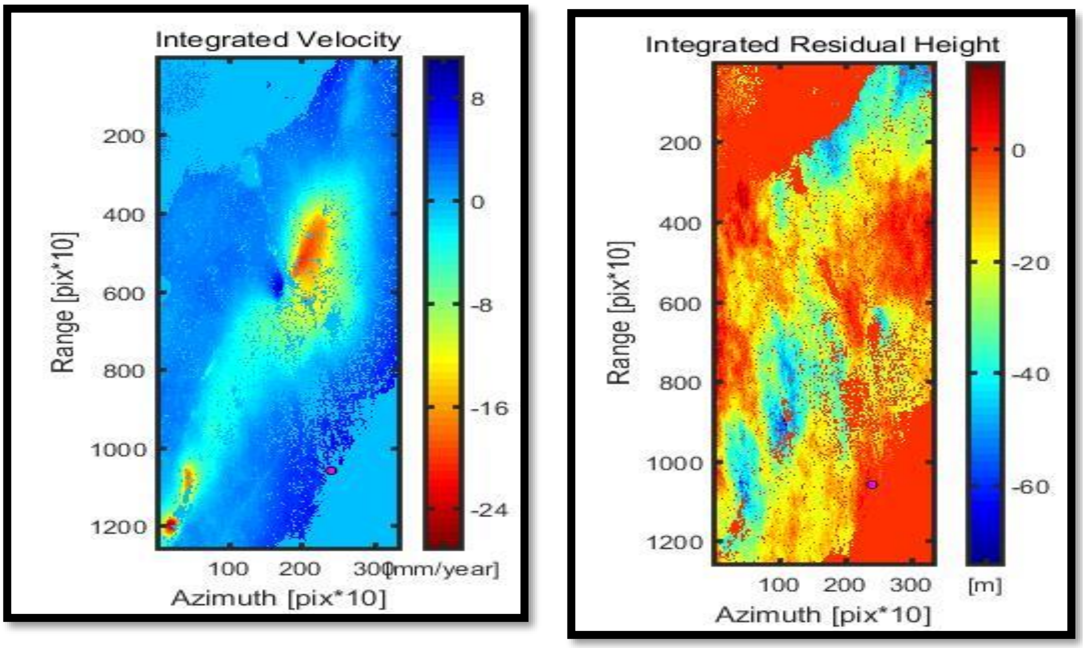

Figure 4. 6 Integrated velocity

Figure 4.5 indicates the cumulative horizontal and vertical displacemet. It is the summation of the displacement from the February 2017 to December 2022. Figure 4.6 is the velocity of the deformation per year.

The map displays horizontal displacement, integrated height, and the rate of deformation within a 20 km radius from the reference point (13.606°, 40.666°).

Evaluation indices for volcanic displacement prediction include the root mean square error (RMSE), coefficient of determination (R^2), these metrics assess the applicability and performance of the displacement prediction model.

$$Root\ mean\ square\ error\ RMS = \sqrt{\frac{1}{n}\sum_{k=1}^{n}(\hat{a}_k - a_k)^2} \qquad 4.1$$

$$Coefficient\ of\ determination\ R^2 = 1 - \frac{\sum_{k=1}^{n}(\hat{a}_k - a_k)^2}{\sum_{k=1}^{n}(\bar{a}_k - a_k)^2} \qquad 4.2$$

Where a_k kth true value of the sample, $\hat{a}_k$ true value of the sample, $\bar{a}k$ is the arithmetic mean of the truth value.

The R^2 and RMSE are calculated from the excel data for cumulative displacement of output are 0.9980 or 99.8% and 6.162e+04. This indicates there high correlation between observed and forecasted data. Figure 4.5 illustrates the cumulative displacement spanning from February 2017 to December 2022, accompanied by a corresponding bar graph on the right side representing PSC along with their respective cumulative displacements. Prominent displacement is observed in regions proximate to active volcanoes, demonstrating a prevailing horizontal deformation pattern oriented in the northwest to southeast direction. Additionally, the ensuing graph presents the cumulative displacement derived from exported Excel data for each PSC.

Moreover, the subsequent representation highlights the peak value of cumulative displacement, achieved through the exclusion of certain data points for refinement.

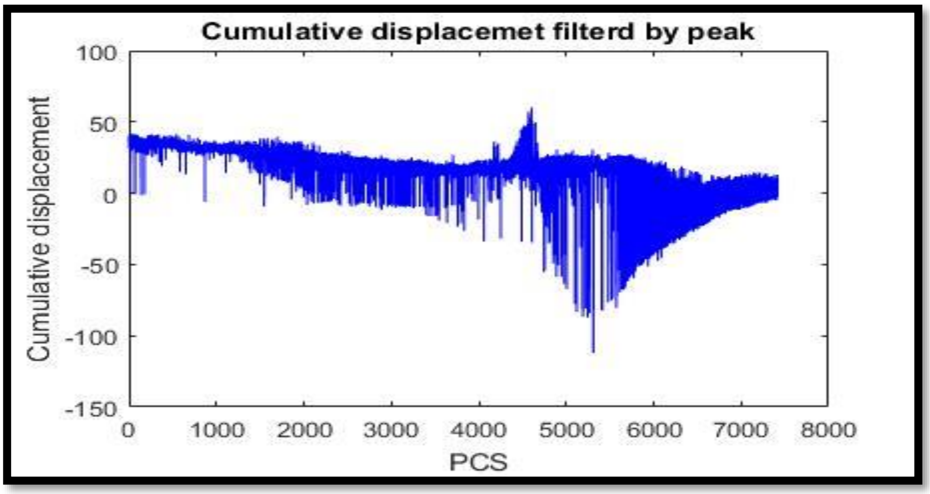

Figure 4. 6 Cumulative displacement of peaks

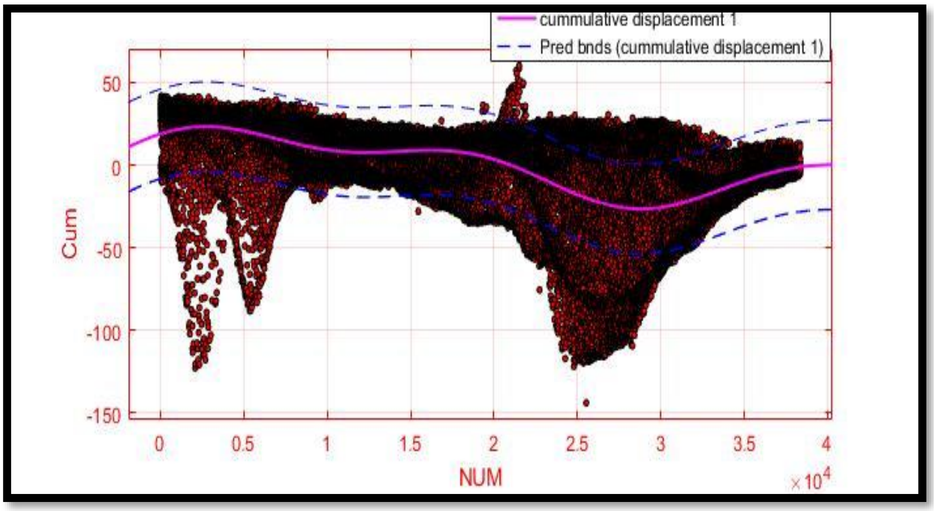

Figure 4. 7 cumulative displacement and its curve fitting

The above figure 4.7 shows the cumulative displacement and the prediction bound. This graph is plotted from the exported excel cumulative displacement from SARPROZ result. The above graphs shows the peak value of the cumulative displacement.

4.1.4 Cumulative Height

A specific objective of this study involves determining vertical displacement from January 2017 to December 2022. Utilizing SARPROZ software, direct assessment of vertical surface changes and their velocities is facilitated. Vertical elevation changes result from the overflow of molten magma during volcanic eruptions, leading to uplift in certain areas and subsidence as magma withdraws at two magma pits.

The subsequent map and accompanying bar graph illustrate the cumulative displacement of the Erta Ale volcano throughout the study period. A 3D map is employed to depict the real topography, serving as a foundation for modeling deformation results. MATLAB is utilized for processing CSV data to establish a model fitting the observed results. In the map, various colors such as cyan, yellow, orange, and blue represent distinct areas. To articulate these results numerically, supplementary analysis is conducted using ArcGIS software.

The 3D map further delineates the mapping of longitude and latitude versus the height of each stable PS) over the years from February 2017 to December 2022. This visualization provides insight into the real ground shape, vertical changes as residuals, and the model of residuals that align with the observed data. Additionally, alongside Google Earth, the final geocoding involves plotting GCP coordinates to generate a 3D topography.

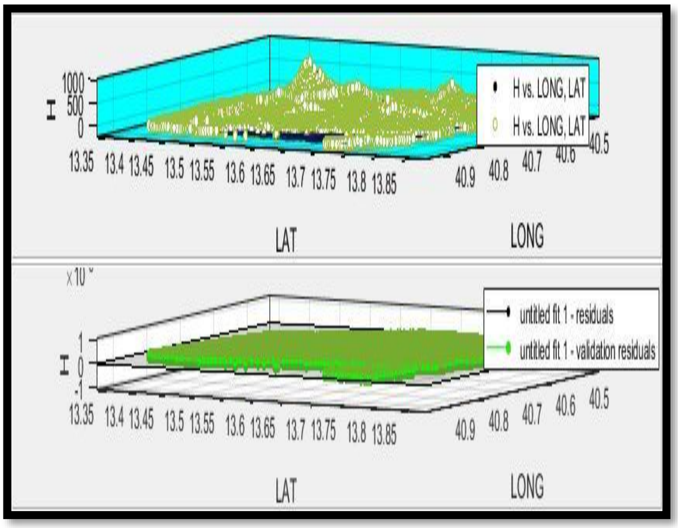

Figure 4. 8 3D plotting of the PSC

The above the figurev shows the 3D representation of the study area for last six study years. The mountainous area is Amayiatoli terara, Borale volcano and other segments found in Erta Ale ridge.

4.1.5 Resampled Displacement

Comparison of any two SAR images reveals resampled displacement during specific study intervals. The ensuing maps portray the modeled residual resampled displacement spanning from February 2017 to December 2022. While both maps present identical results, their differentiation lies in the chosen plotting representation. The subsequent map visualizes the scattered and resampled displacement observed between the reference points in February 2017 and December 2022.

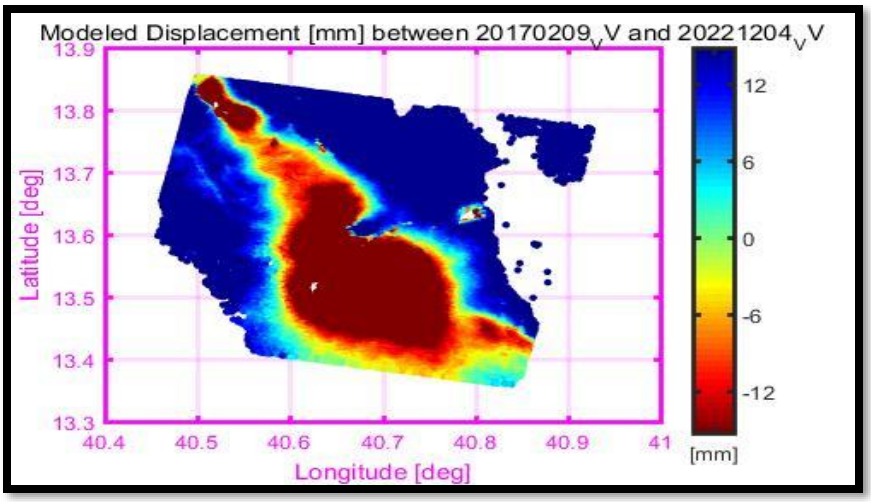

Figure 4. 9 scattered model displacement

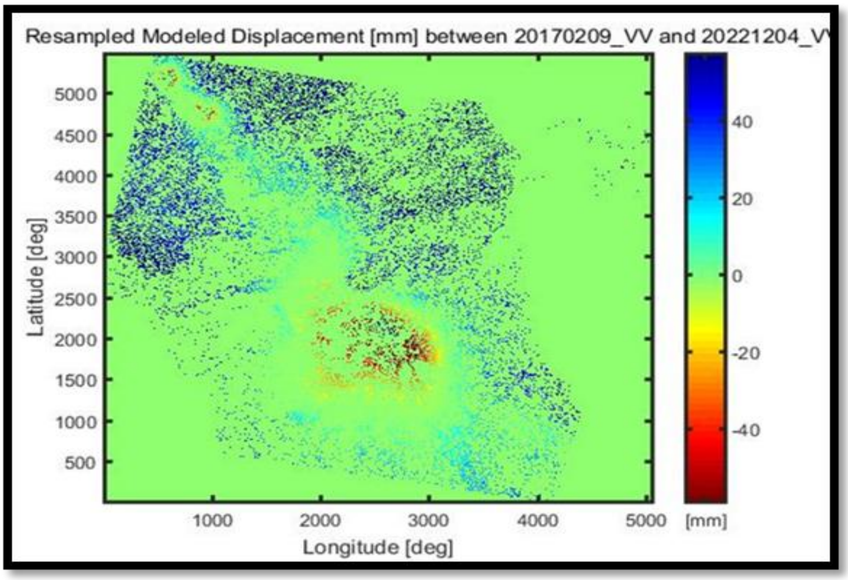

Figure 4. 10 Resampled displacemnet

The above figure 4.9 and 4.10 are the resampled horizontal displacement from the February 2017 to December 2022. Figure 4.9 is scattered displacement where the all displacements are saturated.

4.1.6 Cumulative Velocity

The subsequent maps illustrate deformation velocity, revealing horizontal and vertical ground surface changes across most study areas. The figure below, generated by SARPROZ software, directly depicts the displacement rate per year during the study period's final years.

Table 4. 1 numerical value of final result

Cum.disp uplilft (mm)	Cu.dis.max/ subsid/ (mm)	Vel.max/Uplifting(mm)	Vel. max /subside/(mm)	H. max inflation mm/	H.max Deflation (mm)	Max Sdv
60.23	-143.86	10.3600	-24.7400	93.043	-91.86	5.14

Table 4.1 indicates the maximum value of cumulative displacement, cumulative height and velocity. This value are generated by mathlab using the exported from SARPROZ.

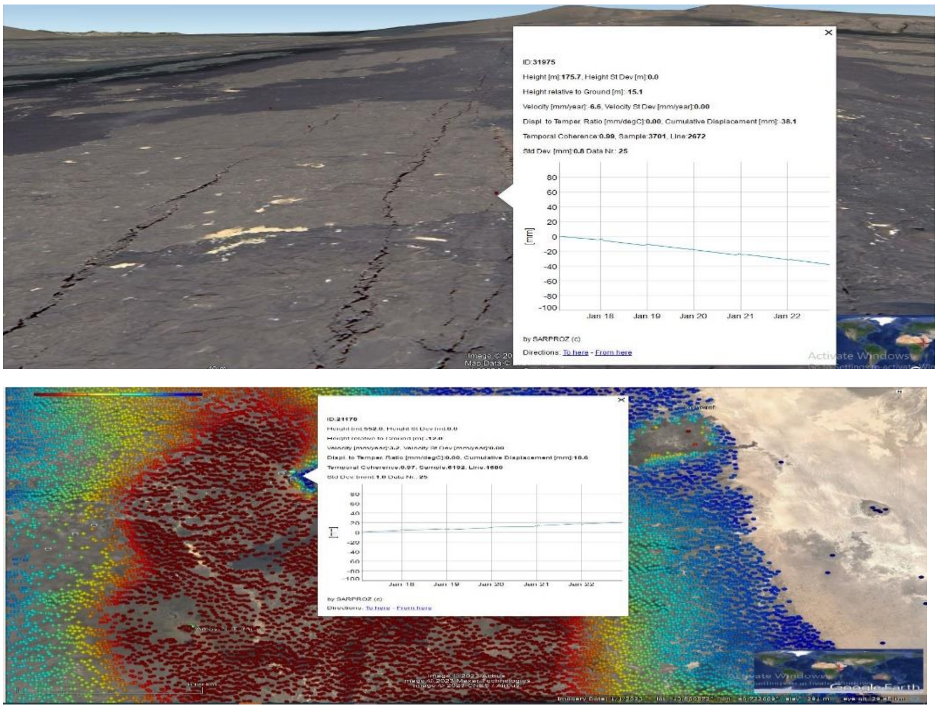

Figure 4. 11 geocoded velocity in google earth

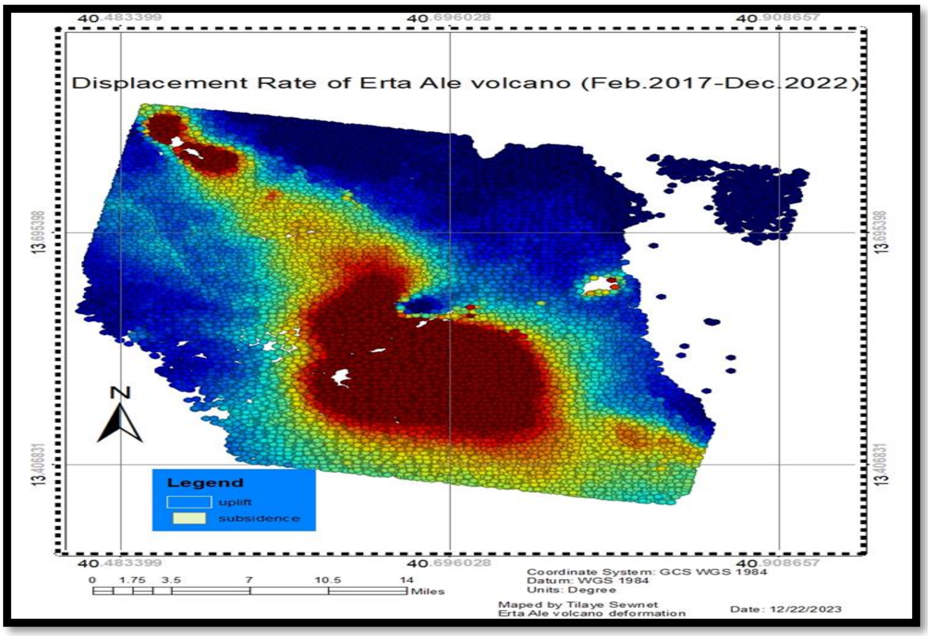

Figure 4. 12 velocity map shape file

Figure 4.11 and 4.12 shows the time series velocity from February 2017 to December 2022 that is created by SARPROZ. To quantify the result is exported to GIS and figure 4.12 shows gis map of velocity time series.

4.2 Discussion

The study utilizes Sentinel 1-A SLC SAR data, a freely available satellite dataset, effective for temporal surface monitoring. The PS method proves efficient in processing SLC data, eliminating phase interference without additional costs. High coherence values signify unchanged ground surfaces, while low coherence indicates alterations, such as vegetation, water, or active lava flows.

Around Erta 'Ale volcano, there is no vegetation and other features that may reduce coherence. Areas where the ground does not change between passes, such as the arid environment around Erta 'Ale and changing surfaces, such as vegetation, water, or active lava flows, resulting in low coherence (Moore et al. 2019). Final displacement map pattern and the direction of deformation can determined using the contrast value. The high coherence value shows a low deformation and the low coherence value shows a high displacement of the place. This is the fact due to the ground surface change, electromagnetic signal reflected from it shows different signal phase values. It also enables to identify area more change occurred in the study period. As the color index of the coherence map shows, the deformed areas have low coherence value.

Interferogram of February 2017 indicates clear that there is deformation to the surface. Onwards from 2017 there are some fringes formed at Erta Ale that are becoming very far spaced or gentle interferogram that except the north lava pits which indicates there is continuous deformation of active magma indicates there is a change in Lava Lake. Around the Erta Ale lava lake reservoir, most areas show gentle fringe color which indicates there small deformation at the surface. The fringe colour sequence indicates that the deformation around the Erta Ale active volcano is the uplifting.

To describe maximum of the subsidence and uplifting deformation in number it is necessary to processes the exported excel data using mat lab. The maximum cumulative velocity of the of uplifting displacement which calculated from the csv excell data exported for each PSC is 10.36±1.2674 mm per year which is around northern pit of the lava lake due to the overflow of magma to the surface. And the maximum cumulative velocity of subsidence is ~24.76±1.2674 mm per year. The average value of deforming rate in Erta Ale volcano is~17.56 mm per year. As we compare this result with (Xu 2020) the difference ~1.56 mm per year, his result shows the spreading rate is ~16 mm/year in the

N77°E direction and have also been recently active. This difference is due to maximum rate of intrusion in both pits resulting the height deflation with maximum rate.

As the graph of displacement shows its maximum horizontal and vertical displacement for uplifting area is ~60.23 ±1.2674 and ~93.04 mm respectively in SW direction resulting horizontal extension of PSC ~1.8cm and vertical uplifting ~9 .04cm. This result is obtained by visualizing the PSC point ID in velocity time series after geocoded in Goggle earth map, this highest values show around pits of volcanos. This result is almost similar with previous (Xu, 2020) result, however the horizontal and vertical uplifting is slightly increasing because still the area is continued with deformation.

In subsidence area the maximum horizontal and vertical displacement are ~143±1.2674 mm and~91.89 mm respectively in N E and some paart of SW direction with deforming rate of ~24.74mm per year by resulting ~18mm contraction of ground horizontally and deflated by ~45m in elevation. As (Xu, 2020) from January 2017 to last 2019 shows maximum horizontal and vertical displacements of ~6 and 9 cm are observed near the northern caldera suggesting they are mainly caused by the contraction of a shallow dike, this almost similar with my result of cumulative displacement for subsidence. The gradual rift-perpendicular contraction and subsidence downs at rates of 50 ± 20 and 5 ± 15 mm/year. The even though deforming rate is decreased by half when we compare with previous study (Xu et al. 2020) from 2017 to 2019 there is subsidence and uplifting in the area until December 2022.

The cumulative displacement is the total summit displacements of each stable point in the whole study years. As the result of the cumulative displacement shows most areas are uplifted in NE and SW direction. The maximum horizontal cumulative displacement in Erta Ale is ~9.cm ±1.2cm. Its map indicates most of the areas around Erta Ale in NE direction are uplifted. The uplifting rate is continuously decreasing when the distance is increase from the two pits. In west direction, Borale or Dalfila volcano causes the uplifting and in SW, direction the over flow of the lava during the eruption causes uplifting. Areas including Bora Ale, Amaytoli Terara, Alybagu and areas in north direction from the Erta Ale N pits are continuously subsiding. In NE-SW, direction of there is continuous opening that causes subsidence. From Erta Ale in north direction there is an opening and continued in NW direction that joined with NW-SE subsidence from Alybagu to BorAle. Between these areas some boreholes and continuous narrow openings that cause contraction of the earth's surface. The subsidence of the area is higher in Borale and Alybagu volcanos and decreases outwards.

The last objective of this thesis is assessing the status of the lava lake of the two pits by comparing the areal change of the initial study year2017 and December 2022. By digitizing Goggle earth map of 2017 and December 2022, I get the areal changes for beginning and end of the study year. The volume of the lava lake of the main Erta Ale is continuously decreasing from 2017 to 2022. The historical map of N pit Lava Lake magma has decreased from ~0.061723km^2 to ~0.036983km^2. This indicates there is high withdrawal of the magma resulting dry magmatic basalt.

To validate the final deformation map, it is necessary to find model that fits the results. To do this I replot csv data using mat lab in the form of graphs or maps. We select two models directly sine2 and polynomial for the plotted (longitude, latitude) versus cumulative displacement map.

General model Sin2: Input data is cumulative displacement plot curve fitting

$$F(x) = a1*\sin(b1*x+c1) + a2*\sin(b2*x+c2) \quad 4.3$$

a1 = 18.96 (18.64, 19.28)

b1 = 0.0001341 (0.0001317, 0.0001364)

c1 = 0.6782 (0.6293, 0.7272)

a2 = 7.842 (7.511, 8.173)

b2 = 0.000349 (0.0003442, 0.0003537

c2 = 1.104 (1.004, 1.204)

Table 4. 2 linear Sum of sine model

Goodness of fit:	SSE	R-square	Adjusted R-square	RMSE
	2.122e+07	0.3094	0.3093	23.52

Chapter Five

5. Conclusion And Recommendation

5.1 Conclusion

This study is about the ground surface deformation at Erta Ale volcano and its surrounding areas using sentiniel-1A SLC data from February 2017 to December 2022. PSI method is effective technique to remove atmospheric phase errors. The final Goggle earth geocoding is good to study the time series displacement and its velocity per stable point during the study time. Atmospheric phase scattering removes the errors in displacement. The rate of deformation (velocity) is decreasing from 2017 to 2022. In Lake Reservoir, there is intrusion, which indicates large withdrawal of the molten magma resulting dry basalt. Due to this area of molten magma is decreasing the area of Lava Lake also decreases. The displacement value per pixel in N and S pits show continuous changes in vertical and horizontal. Most areas around in NE and SW of Erta Ale is uplifting. The northern pit is more deformed than S pit reservoir and the deforming rate of N pit higher than S pits. In geocoded google earth velocity time series map there ground which seems fault that originate near southern pits and some opening halls in NE and E direction resulting subsidence of the ground. This narrow foalt like lines starts from near south of active volcano and continued some distance in SW and at the end area is widened with the same depression pattern. It may be faults or eroded surface; we could not observe it physically to conclude about the opening like line. This needs additional study and investigation. The other thing what observed is there is some surface cracking that may be due to large temperature from the active volcano. This cracking have NE to SW from Alibagu to Borale volcanos that results continuous ground depression. The overall result of the study is similar with previous study at area rather due to its deforming continuity there is some variation on the result. The previous study (Xu et al. 2020) shows more deforming displacement rate than this study. This is due to decreasing the volcanic activity at active volcano. In vertical and horizontal displacement, this study shows slightly greater values than his because still there is deformation at area. The active volcano especially north pits fluctuates in thermal intensity and the area of the magma reservoir is continuously decreasing.

5.2 Recommendations

1. **Recommendation to the user:** The work presented in this paper stems from a geomatics and geodesy perspective, delving into the complexities of volcanic deformation. Further interdisciplinary research is encouraged to gain a comprehensive understanding, possibly incorporating additional analyses.
2. **Recommendation for Researchers:** While this study focuses on a 20 km radius from the northern lava lake, future research should expand its scope to investigate the impacts of deformation on neighboring natural and artificial features. Conducting additional studies covering larger areas, including the surrounding regions, would contribute to a more comprehensive analysis.

Reference

Achmad, Arief Rizqiyanto, and Chang Wook Lee. 2021. “Surface Deformation Measurement of the 2020 Mw 6.4 Petrinja, Croatia Earthquake Using Sentinel-1 SAR Data.” Korean Journal of Remote Sensing 37(1):139–51.doi: 10.7780/kjrs.2021.37.1.11.

Albino, F., J. Biggs, C. Yu, and Z. Li. n.d. “Automated Methods for Detecting Volcanic Deformation Using Sentinel-1 InSAR Time Series Illustrated by the 2017-2018 Unrest at Agung, Indonesia.” doi: 10.1029/2019JB017908.

Albino, Fabien, Juliet Biggs, Milan Lazecký, and Yasser Maghsoudi. 2022. “Routine Processing and Automatic Detection of Volcanic Ground Deformation Using Sentinel-1 InSAR Data: Insights from African Volcanoes.” Remote Sensing 14(22):1–20. doi: 10.3390/rs14225703.

Anon. 2002. “Stochastic Model for Radar Interferometry.” 81–159.

Anon. n.d.-a. “Goldstein_RadioSci1988.Pdf.”

Anon. n.d.-b. Processing of SAR Data Synthetic Aperture Radar.II Series.

Bagnardi, Marco, and Andrew Hooper. 2018. “Inversion of Surface Deformation Data for Rapid Estimates of Source Parameters and Uncertainties: A Bayesian Approach.” Geochemistry, Geophysics, Geosystems 19(7):2194–2211. doi: 10.1029/2018GC007585.

Bamler, R. 2000. “Principles of Synthetic Aperture Radar.” Surveys in Geophysics 21(2–3):147–57. doi: 10.1023/A:1006790026612.

Barberi, F., and J. Varet. n.d. “The Erta Ale Volcanic Range (Danakil Depression , Northern Afar , Ethiopia) The Afar (or Danakil) Depression Is One of the Key Regions For.”

Barnie, T. D., C. Oppenheimer, and C. Pagli. 2016. “Does the Lava Lake of Erta ’Ale Volcano Respond to Regional Magmatic and Tectonic Events? An Investigation Using Earth Observation Data.” Geological Society Special Publication 420(1):181–208. doi: 10.1144/SP420.15.

Beal, Robert C. 1979. “Useful Spaceborne Synthetic Aperture Radars.” Astronautics for Peace and Human Progress 263–75. doi: 10.1016/b978-0-08-024732-8.50026-x.

Beyene, Alebachew, and Mohamed G. Abdelsalam. 2005. “Tectonics of the Afar Depression: A Review and Synthesis.” Journal of African Earth Sciences 41(1–2):41–59. doi: 10.1016/j.jafrearsci.2005.03.003.

Bonini, Marco, Giacomo Corti, Fabrizio Innocenti, Piero Manetti, Francesco Mazzarini, Tsegaye Abebe, and Zoltan Pecskay. 2005. “Evolution of the Main Ethiopian Rift in the Frame of Afar and Kenya Rifts Propagation.” Tectonics 24(1):1–21. doi: 10.1029/2004TC001680.

Borghero, Cecilia. 2017. “Feasibility Study of Dam Deformation Monitoring in Northern Sweden Using Sentinel1 SAR Interferometry.” 77.

Braun, Andreas, and Eric Offermann. 2022. “Polarimetric Information Content of Sentinel-1 for Land Cover Mapping: An Experimental Case Study Using Quad-Pol Data Synthesized from Complementary Repeat-Pass Acquisitions.” Frontiers in Remote Sensing 3(September):1–22. doi: 10.3389/frsen.2022.905713.

Chan, Y. K., and V. C. Koo. 2008. “An Introduction to Synthetic Aperture Radar (SAR).” Progress In Electromagnetics Research B 2:27–60. doi: 10.2528/pierb07110101.

Chen, Curtis W., and Howard A. Zebker. 2002. “Phase Unwrapping for Large SAR Interferograms : Statistical Segmentation and Generalized Network Models.” 40(8):1709–19.

Chernet, Tadiwos, William K. Hart, James L. Aronson, and Robert C. Walter. 1998. “New Age Constraints on the Timing of Volcanism and Tectonism in the Northern Main Ethiopian Rift - Southern Afar Transition Zone (Ethiopia).” Journal of Volcanology and Geothermal Research 80(3–4):267–80. doi: 10.1016/S0377-0273(97)00035-8.

Cong, Xiaoying, Ulrich Balss, Fernando Rodriguez Gonzalez, and Michael Eineder. 2018. “Mitigation of Tropospheric Delay in SAR and InSAR Using NWP Data: Its Validation and Application Examples.” Remote Sensing 10(10):1–21. doi: 10.3390/rs10101515.

Crosetto, Michele, Oriol Monserrat, María Cuevas-González, Núria Devanthéry, and Bruno Crippa. 2016. “Persistent Scatterer Interferometry: A Review.” ISPRS Journal of Photogrammetry and Remote Sensing 115:78–89. doi:

10.1016/j.isprsjprs.2015.10.011.

Data, Ground-based S. A. R., and Yuta Izumi. 2023. “Evaluation of Atmospheric Phase Correction Performance in 79 GHz Ground-Based Radar Interferometry : A Comparison.”

Deledalle, Charles Alban, Loïc Denis, and Florence Tupin. 2011. “NL-InSAR: Nonlocal Interferogram Estimation.” IEEE Transactions on Geoscience and Remote Sensing 49(4):1441–52. doi: 10.1109/TGRS.2010.2076376.

Dobkin, David P., Steven J. Friedman, and Kenneth J. Supowit. 1987. “Delaunay Graphs Are Almost As Good As Complete Graphs.” Annual Symposium on Foundations of Computer Science (Proceedings) 20–26. doi: 10.1109/sfcs.1987.18.

Doubre, Cécile, Aline Déprez, Frédéric Masson, Anne Socquet, Elias Lewi, Raphaël Grandin, Alexandre Nercessian, Patrice Ulrich, Jean Bernard De Chabalier, Ibrahim Saad, Ahmadine Abayazid, Gilles Peltzer, Arthur Delorme, Eric Calais, and Tim Wright. 2017. “Current Deformation in Central Afar and Triple Junction Kinematics Deduced from GPS and InSAR Measurements.” Geophysical Journal International 208(2):936–53. doi: 10.1093/gji/ggw434.

Externe, Rapporteur, Rapporteur Externe, and Rapporteur Interne. 2013. “Présentée à L ’ Université de Strasbourg Pour l ’ Obtention Du Grade de : Discipline : Science de La Terre et de l ’ U Nivers Spécialité : Géophysique Time Series Analysis of SAR Images Using Persistent Scatterer (PS), Small Baseline (SB) and Merged A.”

Ferretti, Alessandro, Claudio Prati, and Fabio Rocca. 2001. “Permanent Scatterers in SAR Interferometry.” IEEE Transactions on Geoscience and Remote Sensing 39(1):8–20. doi: 10.1109/36.898661.

Field, Lorraine, Talfan Barnie, Jon Blundy, Richard A. Brooker, Derek Keir, Elias Lewi, and Kate Saunders. 2012. “Integrated Field, Satellite and Petrological Observations of the November 2010 Eruption of Erta Ale.” Bulletin of Volcanology 74(10):2251–71. doi: 10.1007/s00445-012-0660-7.

Fornaro, G., A. Monti Guarnieri, A. Pauciullo, and F. De-Zan. 2006. “Maximum Likelihood Multi-Baseline SAR Interferometry.” IEE Proceedings: Radar, Sonar and Navigation 153(3):279–88. doi: 10.1049/ip-rsn:20045113.

Gehlot, S., V. B. H. Ketelaar, E. Verbree, and R. F. Hanssen. 2005. “Conceptual

Framework for {PS-InSAR} Deformation Interpretation Assisted by Geo-Information Technology.” ISPRS Workshop, High-Resolution Earth Imaging for Geospatial Information, Hannover, Germany, 17--20 May 2005 5.

Goldstein, Richard M., and Charles L. Werner. 1998. “Radar Interferogram Filtering for Geophysical Applications.” Geophysical Research Letters 25(21):4035–38. doi: 10.1029/1998GL900033.

Grandin, R., A. Socquet, E. Jacques, N. Mazzoni, J. B. De Chabalier, and G. C. P. King. 2010. “Sequence of Rifting in Afar, Manda-Hararo Rift, Ethiopia, 2005-2009: Time-Space Evolution and Interactions between Dikes from Interferometric Synthetic Aperture Radar and Static Stress Change Modeling.” Journal of Geophysical Research: Solid Earth 115(10):2005–9. doi: 10.1029/2009JB000815.

Guanabara, Editora, Koogan Ltda, Editora Guanabara, and Koogan Ltda. n.d. NoTitle.

Guarango, Piedad Magali. 2022. “No Title(8.5.2017):2003–5.

Gudmundsson, Agust. 2020. Volcanotectonic Processes.

Habte, A. 2021. “Determination of Crustal Deformation around Afar (Erta Ale) Using Sentinel 1 SAR Interferometry.” 10(1000):1–7.

Hagos, Miruts, Christian Koeberl, and Benjamin van Wyk de Vries. 2016. “The Quaternary Volcanic Rocks of the Northern Afar Depression (Northern Ethiopia): Perspectives on Petrology, Geochemistry, and Tectonics.” Journal of African Earth Sciences 117:29–47. doi: 10.1016/j.jafrearsci.2015.11.022.

Hamling, Ian J., Tim J. Wright, Eric Calais, Elias Lewi, and Yukitoshi Fukahata. 2014. “InSAR Observations of Post-Rifting Deformation around the Dabbahu Rift Segment, Afar, Ethiopia.” Geophysical Journal International 197(1):33–49. doi: 10.1093/gji/ggu003.

Hammond, J. O. S., J. M. Kendall, G. W. Stuart, D. Keir, C. Ebinger, A. Ayele, and M. Belachew. 2011. “The Nature of the Crust beneath the Afar Triple Junction: Evidence from Receiver Functions.” Geochemistry, Geophysics, Geosystems 12(12). doi: 10.1029/2011GC003738.

Hatton, Emma. 2020. “Displacements Monitoring over Czechia by IT4S1 System for Automatised Interferometric Measurements Using Sentinel-1 Data.” 1–21.

Iglesias, Ruben, Xavier Fabregas, Albert Aguasca, Jordi J. Mallorqui, Carlos Lopez-Martinez, Josep A. Gili, and Jordi Corominas. 2014. “Atmospheric Phase Screen Compensation in Ground-Based Sar with a Multiple-Regression Model over Mountainous Regions.” IEEE Transactions on Geoscience and Remote Sensing 52(5):2436–49. doi: 10.1109/TGRS.2013.2261077.

Izumi, Yuta, Othmar Frey, Simone Baffelli, Irena Hajnsek, and Motoyuki Sato. 2021. “Efficient Approach for Atmospheric Phase Screen Mitigation in Time Series of Terrestrial Radar Interferometry Data Applied to Measure Glacier Velocity.” IEEE Journal of Selected Topics in Applied Earth Observations and Remote Sensing 14:7734–50. doi: 10.1109/JSTARS.2021.3099873.

Jia, Hongguo, and Luyao Liu. 2016. “A Technical Review on Persistent Scatterer Interferometry.” Journal of Modern Transportation 24(2):153–58. doi: 10.1007/s40534-016-0108-4.

Jiang, Yu, and Pablo J. González. 2020. “Bayesian Inversion of Wrapped Satellite Interferometric Phase to Estimate Fault and Volcano Surface Ground Deformation Models.” Journal of Geophysical Research: Solid Earth 125(5). doi: 10.1029/2019JB018313.

Khalili, Mohammad Amin, Behzad Voosoghi, Luigi Guerriero, and Saeid Haji-aghajany. 2023. “Mapping of Mean Deformation Rates Based on APS-Corrected InSAR Data Using Unsupervised Clustering Algorithms.”

Kim, Jin Woo. 2013. “Applications of Synthetic Aperture Radar (SAR)/ SAR Interferometry (InSAR) for Monitoring of Wetland Water Level and Land Subsidence.” Ohio State University (503):1–111.

Krieger, Gerhard, Irena Hajnsek, Konstantinos Panagiotis Papathanassiou, Marwan Younis, and Alberto Moreira. 2010. “Interferometric Synthetic Aperture Radar (SAR) Missions Employing Formation Flying.” Proceedings of the IEEE 98(5):816–43. doi: 10.1109/JPROC.2009.2038948.

Kumar, U., C. P. Legendre, and B. S. Huang. 2021. “Crustal Structure and Upper Mantle Anisotropy of the Afar Triple Junction.” Earth, Planets and Space 73(1). doi: 10.1186/s40623-021-01495-0.

Lafayette, West. n.d. “Image Coregistration in Sar Interferometry.”

Lanari, Riccardo, Francesco Casu, Mariarosaria Manzo, Giovanni Zeni, Paolo Berardino, Michele Manunta, and Antonio Pepe. 2007. "An Overview of the Small BAseline Subset Algorithm: A DInSAR Technique for Surface Deformation Analysis." Pure and Applied Geophysics 164(4):637–61. doi: 10.1007/s00024-007-0192-9.

Lee, D. T., and A. K. Lin. 1986. "Generalized Delaunay Triangulation for Planar Graphs." Discrete & Computational Geometry 1(1):201–17. doi: 10.1007/BF02187695.

Lemenkova, Polina. 2022. "Seismicity in the Afar Depression and Great Rift Valley, Ethiopia." Environmental Research, Engineering and Management 78(1):83–96. doi: 10.5755/j01.erem.78.1.29963.

Li, Tao, Yuanlin Hu, Bin Liu, Liming Jiang, Hansheng Wang, and Xiang Shen. 2022. "Co-Registration and Residual Correction of Digital Elevation Models: A Comparative Study." The Cryosphere Discuss - Preprint (November):1–22.

Liu, Youfeng, Honglei Yang, Shizheng Wang, Linlin Xu, and Junhuan Peng. 2022. "Monitoring and Stability Analysis of the Deformation in the Woda Landslide Area in Tibet, China by the DS-InSAR Method." Remote Sensing 14(3). doi: 10.3390/rs14030532.

Lu, Zhong, Dörte Mann, Jeffrey T. Freymueller, and David J. Meyer. 2000. "Synthetic Aperture Radar Interferometry of Okmok Volcano, Alaska: Radar Observations." Journal of Geophysical Research: Solid Earth 105(B5):10791–806. doi: 10.1029/2000jb900034.

Mancini, Francesco, Francesca Grassi, and Nicola Cenni. 2021. "A Workflow Based on Snap–Stamps Open-source Tools and Gnss Data for Psi-based Ground Deformation Using Dual-orbit Sentinel-1 Data: Accuracy Assessment with Error Propagation Analysis." Remote Sensing 13(4):1–23. doi: 10.3390/rs13040753.

Marghany, Maged. 2020. "Principles of Synthetic Aperture Radar." Advanced Remote Sensing Technology for Tsunami Modelling and Forecasting 223–39. doi: 10.1201/9781351175548-18.

Martínek, Karel, Kryštof Verner, Tomáš Hroch, Leta A. Megerssa, David Buriánek, Ameha Muluneh, Radka Kalinová, and Miheret Yakob. 2021. "Main Ethiopian Rift Landslides Formed in Contrasting Geological." (January).

Melvin, William L., and James A. Scheer. 2013. Principles of Modern Radar: Advanced Techniques.

Monti-Guarnieri, Andrea, Fabio Rocca, and Stefano Tebaldini. 2018. SAR Interferometry.

Moore, C., T. Wright, and A. Hooper. 2020. “Rift Focussing and Magmatism During Late-Stage Rifting in Afar , Ethiopia.” 1–19.

Moore, C., T. Wright, A. Hooper, and J. Biggs. 2019. “The 2017 Eruption of Erta ’Ale Volcano, Ethiopia: Insights Into the Shallow Axial Plumbing System of an Incipient Mid-Ocean Ridge.” Geochemistry, Geophysics, Geosystems 20(12):5727–43. doi: 10.1029/2019GC008692.

Mora, Oscar, Roman Arbiol, and Vicenç Palà. 2006. “Advanced DInSAR Techniques for Monitoring Terrain Displacements.” 5th European Congress on Regional Geoscientific … (Icc):324–26.

Nobile, Adriano. n.d. “Volcano Deformation in Different Tectonic Settings Using InSAR and Modeling.”

Osmanoğlu, Batuhan, Filiz Sunar, Shimon Wdowinski, and Enrique Cabral-Cano. 2016. “Time Series Analysis of InSAR Data: Methods and Trends.” ISPRS Journal of Photogrammetry and Remote Sensing 115:90–102. doi: 10.1016/j.isprsjprs.2015.10.003.

Oštir, Krištof, and Marko Komac. 2007. “PSInSAR and DInSAR Methodology Comparison and Their Applicability in the Field of Surface Deformations–A Case of NW Slovenia.” Geologija 50(1):77–96. doi: 10.5474/geologija.2007.007.

Pepe, Antonio, and Fabiana Calò. 2017. “A Review of Interferometric Synthetic Aperture RADAR (InSAR) Multi-Track Approaches for the Retrieval of Earth’s Surface Displacements.” Applied Sciences (Switzerland) 7(12). doi: 10.3390/app7121264.

Pritchard, Matthew E., and Mark Simons. 2002. “A Satellite Geodetic Survey of Large-Scale Deformation of Volcanic Centres in the Central Andes.” Nature 418(6894):167–71. doi: 10.1038/nature00872.

Pu, Liming, Xiaoling Zhang, Zenan Zhou, Jun Shi, Shunjun Wei, and Yuanyuan Zhou.

2020. “A Phase Filtering Method with Scale Recurrent Networks for InSAR.” Remote Sensing 12(20):1–25. doi: 10.3390/rs12203453.

Puglisi, G., and M. Coltelli. 2001. “SAR Interferometry Applications on Active Volcanoes: State of the Art and Perspectives for Volcano Monitoring.” Nuovo Cimento Della Societa Italiana Di Fisica C 24(1):133–45.

Redadda, S., A. Boualleg, and R. Hamdi. 2009. “An Analysis of Topographic InSAR Algorithms.” Differentiation 1–8.

RI, MENTERI KESEHATAN. 2019. “No TitleΕΛΕΝΗ.” Αγαη 8(5):55.

Rongier, Guillaume, Cody Rude, Thomas Herring, and Victor Pankratius. 2019. “Generative Modeling of InSAR Interferograms.” Earth and Space Science 6(12):2671–83. doi: 10.1029/2018EA000533.

Samsonov, Sergey, Kristy Tiampo, Pablo J. Gonzalez, Juan Prieto, Antonio G. Camacho, and José Fernández. 2008. “Surface Deformation Studies of Tenerife Island, Spain from Joint GPS-DInSAR Observations.” Proceedings of the 2008 2nd Workshop on USE of Remote Sensing Techniques for Monitoring Volcanoes and Seismogenic Areas, USEReST 2008 1–6. doi: 10.1109/USEREST.2008.4740337.

Simons, M., and P. A. Rosen. 2015. Interferometric Synthetic Aperture Radar Geodesy. Vol. 3. Elsevier B.V.

Soumekh, Mehrdad. n.d. “Synthetic Aperture Radar Signal Processing with MATLAB Algorithms.”

Staniewicz, Scott, Jingyi Chen, Hunjoo Lee, Jon Olson, Alexandros Savvaidis, Robert Reedy, Caroline Breton, Ellen Rathje, and Peter Hennings. 2020. “InSAR Reveals Complex Surface Deformation Patterns Over an 80,000 Km2 Oil-Producing Region in the Permian Basin.” Geophysical Research Letters 47(21). doi: 10.1029/2020GL090151.

Suwarsono, D. Triyono, M. R. Khomarudin, and Rokhmatuloh. 2020. “Surface Deformation Due to the 2017-2018 Agung Volcano Eruption from Interferometric Synthetic Aperture Radar (InSAR) Sentinel-1 TOPS.” Journal of Physics: Conference Series 1577(1). doi: 10.1088/1742-6596/1577/1/012055.

Tang, Xiaoyu, Wen Wan, Zongtang Zhang, Wenhua Gao, and Yanhao Wang. 2023.

“Residual Deformation of Coal Gangue Subgrade Filler under Multi-Vibration Cyclic Loading.” Scientific Reports 13(1):1–15. doi: 10.1038/s41598-023-35199-0.

Thamaria, Netty, and Unigarro et al. 2005. “No 主観的健康感を中心とした在宅高齢者における 健康関連指標に関する共分散構造分析Title.” Journal of Chemical Information and Modeling 12 Suppl 1(9):1–29.

Tian, Xin, Rakesh Malhotra, Bing Xu, Haoping Qi, and Yuxiao Ma. 2018. “Modeling Orbital Error in InSAR Interferogram Using Frequency and Spatial Domain Based Methods.” Remote Sensing 10(4):1–14. doi: 10.3390/rs10040508.

Tzouvaras, Marios, Chris Danezis, and Diofantos G. Hadjimitsis. 2020. “Differential SAR Interferometry Using Sentinel-1 Imagery-limitations in Monitoring Fast Moving Landslides: The Case Study of Cyprus.” Geosciences (Switzerland) 10(6):1–26. doi: 10.3390/geosciences10060236.

Universitaria, Ciudad, Indra Espacio, Mar Egeo, San Fernando, San Urbano, Museo Nacional, and Ciencias Naturales. 2002. “Sar): A.” 55–84.

Varet, Jacques. 2018. Geology of Afar (East Africa).

Victor C. Che and Marco Martorella. n.d. No Title.

Wang, Teng, Sigurjón Jónsson, and Ramon Hanssen. 2012. “Coregistration between Sar Image Subsets Using Pointwise Targets.” 2011(January):19–23.

Wang, Yuyi, Yahui Guo, Shunqiang Hu, Yong Li, Jingzhe Wang, Xuesong Liu, and Le Wang. 2019. “Ground Deformation Analysis Using InSAR and Backpropagation Prediction with Influencing Factors in Erhai Region, China.” Sustainability (Switzerland) 11(10). doi: 10.3390/su11102853.

Wolfenden, Ellen, Cynthia Ebinger, Gezahegn Yirgu, Alan Deino, and Dereje Ayalew. 2004. “Evolution of the Northern Main Ethiopian Rift: Birth of a Triple Junction.” Earth and Planetary Science Letters 224(1–2):213–28. doi: 10.1016/j.epsl.2004.04.022.

Xia, Ye. 2010a. “Synthetic Aperture Radar Interferometry.” Sciences of Geodesy - I: Advances and Future Directions 1:415–74. doi: 10.1007/978-3-642-11741-1_11.

Xia, Ye. 2010b. “Synthetic Aperture Radar Interferometry.” Sciences of Geodesy - I: Advances and Future Directions 14:415–74. doi: 10.1007/978-3-642-11741-1_11.

Xu, Wenbin. 2020. “Volcano - Wide Deformation After the 2017 Erta Ale Dike Intrusion , Ethiopia , Observed With Radar Interferometry Journal of Geophysical Research : Solid Earth.” doi: 10.1029/2020JB019562.

Xu, Wenbin, Eleonora Rivalta, and Xing Li. 2017. “Magmatic Architecture within a Rift Segment: Articulate Axial Magma Storage at Erta Ale Volcano, Ethiopia.” Earth and Planetary Science Letters 476:79–86. doi: 10.1016/j.epsl.2017.07.051.

Xu, Wenbin, Lei Xie, Yosuke Aoki, Eleonora Rivalta, and Sigurjón Jónsson. 2020. “Volcano-Wide Deformation After the 2017 Erta Ale Dike Intrusion, Ethiopia, Observed With Radar Interferometry.” Journal of Geophysical Research: Solid Earth 125(8). doi: 10.1029/2020JB019562.

Yamaguchi, Yoshio. 2020. Polarimetric Synthetic Aperture Radar.

Younis, Marwan. 2020. “Synthetic Aperture Radar (SAR) Techniques and Applications.” Synthetic Aperture Radar (SAR) Techniques and Applications. doi: 10.3390/books978-3-03936-123-6.

Yu, Qifeng, Sihua Fu, Helmut Mayer, Xiaolin Liu, and Xia Yang. 2007. “Coregistration Based on Three Parts of Two Complex Images and Contoured Windows for Synthetic Aperture Radar Interferometry.” 4(2):288–92.

Zebker, Howard A., and John Villasenor. 1992. “Decorrelation in Interferometric Radar Echoes.” IEEE Transactions on Geoscience and Remote Sensing 30(5):950–59. doi: 10.1109/36.175330.

Zwaan, F., G. Corti, F. Sani, D. Keir, A. A. Muluneh, F. Illsley-Kemp, and M. Papini. 2020. “Structural Analysis of the Western Afar Margin, East Africa: Evidence for Multiphase Rotational Rifting.” Tectonics 39(7):1–25. doi: 10.1029/2019TC006043.

Zwaan, Frank, Giacomo Corti, Derek Keir, and Federico Sani. 2020. “A Review of Tectonic Models for the Rifted Margin of Afar: Implications for Continental Break-up and Passive Margin Formation.” Journal of African Earth Sciences 164. doi: 10.1016/j.jafrearsci.2019.103649.

Appendix

Table Apendex 1

no	Item class: SENTINEL-1A Interferometric Wide Swath Level 1 S Product	Date of acquisition	Elapsed time
1	S1A_IW_SLC__1SDV_20170209T030748_20170209T030815_015201_018E37_C90D.SAFE	2017-02-09T05:12:54	1.372
2	S1A_IW_SLC__1SDV_20170221T030748_20170221T030815_015376_0193AB_1E98.SAFE	2017-02-21T05:17:07	1.23
3	S1A_IW_SLC__1SDV_20171218T030756_20171218T030823_019751_021960_3ACA.SAFE	2017-12-18T05:19:51	1.324
4	S1A_IW_SLC__1SDV_20180111T030755_20180111T030822_020101_022454_3DD4.SAFE	2018-01-11T05:35:32	1.538
5	S1A_IW_SLC__1SDV_20180123T030755_20180123T030822_020276_0229E2_6206.SAFE	2018-01-23T05:30:17	1.205
6	S1A_IW_SLC__1SDV_20181213T030803_20181213T030830_025001_02C1B6_3C60.SAFE	2018-12-13T08:46:11	0.941
7	S1A_IW_SLC__1SDV_20181225T030802_20181225T030829_025176_02C80C_0727.SAFE	2018-12-25T07:00:31	1.133
8	S1A_IW_SLC__1SDV_20190106T030802_20190106T030829_025351_02CE5B_9507.SAFE	2019-01-06T05:52:42	1.155
9	S1A_IW_SLC_1SDV_20181225T030802_20181225T030829_025176_02C80C_0727.SAFE	2018-12-25T07:00:31	1.133
10	S1A_IW_SLC__1SDV_20190118T030802_20190118T030829_025526_02D4AB_CCF6.SAFE	2019-01-18T05:41:57	1.248
11	S1A_IW_SLC_1SDV_20190424T030802_20190424T030829_026926_030779_0A76.SAFE	2019-04-24T06:07:	1.25
12	S1A_IW_SLC__1SDV_20190130T030801_20190130T030828_025701_02DB13_1D00.SAFE	2019-01-30T05:37:57	0.765
13	S1A_IW_SLC__1SDV_20191220T030809_20191220T030836_030426_037B6B_9D8A.SAFE	2019-12-20T06:58:12	0.778

Table Apendex 1

No	**Item class:** SENTINEL-1A Interferometric Wide Swath Level 1 S Product	Date of acquisition	Elapsed time
14	S1A_IW_SLC__1SDV_20200101T030808_20200101T030835_030601_038176_04FC.SAF	2020-01-01T08:39:48	0.769
15	S1A_IW_SLC__1SDV_20200113T030808_20200113T030835_030776_03878A_D155.SAFE	2020-01-13T08:44:29	1.066
16	S1A_IW_SLC__1SDV_20200125T030808_20200125T030835_030951_038DB5_F9F1.SAFE	2020-01-25T08:33:59	0.68
17	S1A_IW_SLC__1SDV_20201202T030816_20201202T030843_035501_042684_928F.SAFE	2020-12-02T07:05:27	1.355
18	S1A_IW_SLC__1SDV_20201214T030816_20201214T030842_035676_042C85_2926.SAFE	2020-12-14T06:14:32	1.006
19	S1A_IW_SLC__1SDV_20201226T030815_20201226T030842_035851_043291_CA02.SAFE	2020-12-26T08:49:10	0.891
20	S1A_IW_SLC__1SDV_20210107T030814_20210107T030841_036026_0438A5_E272.SAFE	2021-01-07T12:36:08	0.906
21	S1A_IW_SLC__1SDV_20210119T030814_20210119T030841_036201_043ECD_1012.SAFE	2021-01-19T07:05:04	1.14
22	S1A_IW_SLC__1SDV_20210131T030813_20210131T030840_036376_0444DB_775B.SAFE	2021-01-31T07:01:00	1.58
23	S1A_IW_SLC__1SDV_20211221T030821_20211221T030848 _041101_04E20D_AC49.SAFE	2022-06-07T03:08	0.682
24	S1A_IW_SLC__1SDV_20220114T030820_20220114T030847 _041451_04EDAF_2EC8.SAFE	2022-01-14 T03:08	0.705
25	S1A_IW_SLC__1SDV_20220126T030819_20220126T030846 _041626_04F3AA_83FA.SAFE	2022-01-26T03:08:46	0.694
26	S1A_IW_SLC__1SDV_20221204T030828_20221204T030854 _046176_058748_2579.SAFE	2022-12-04T03:08:54	0.628

Appendix 2 Figure

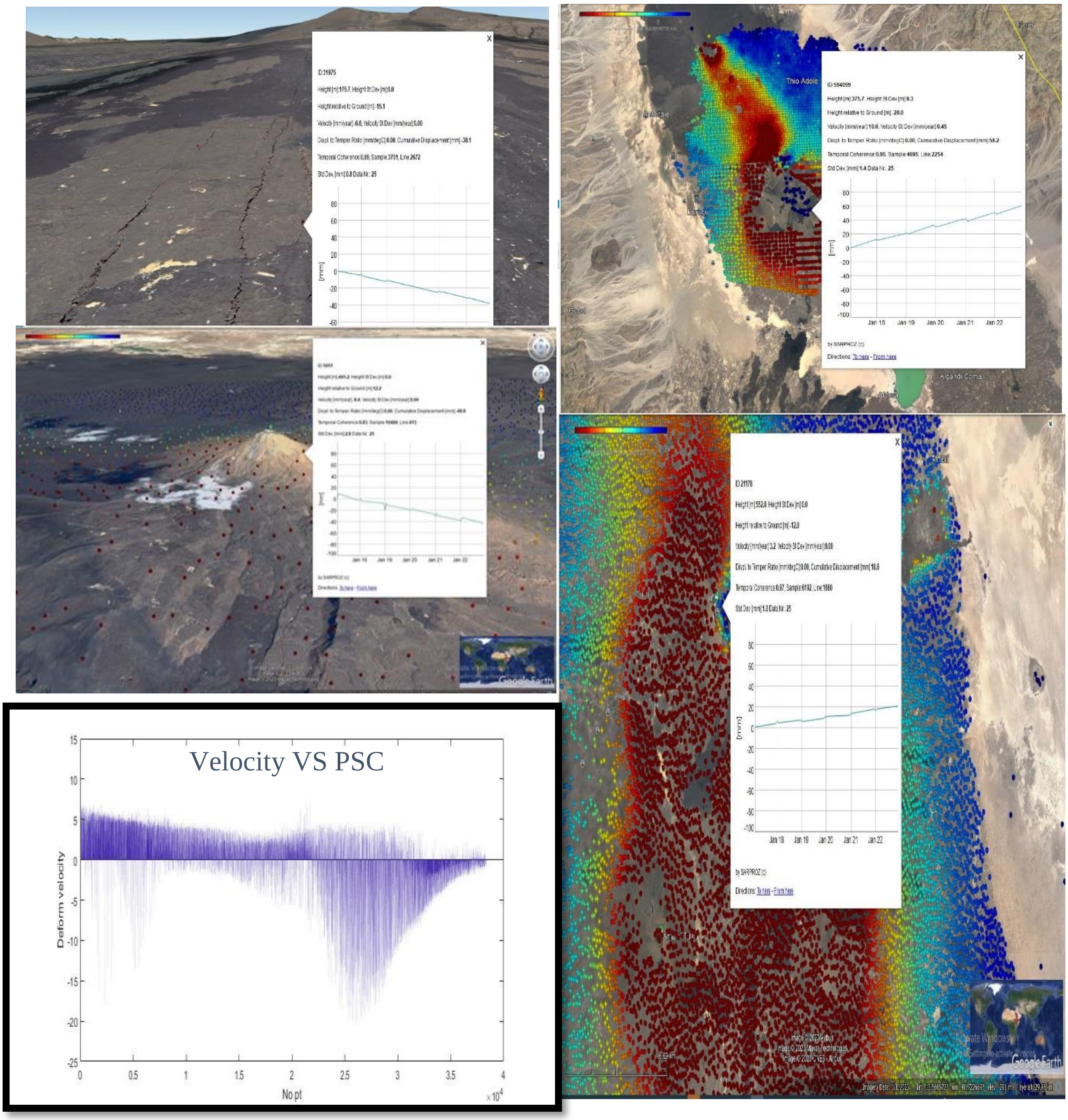

Figure 3. 1 Baseline distance from the master image

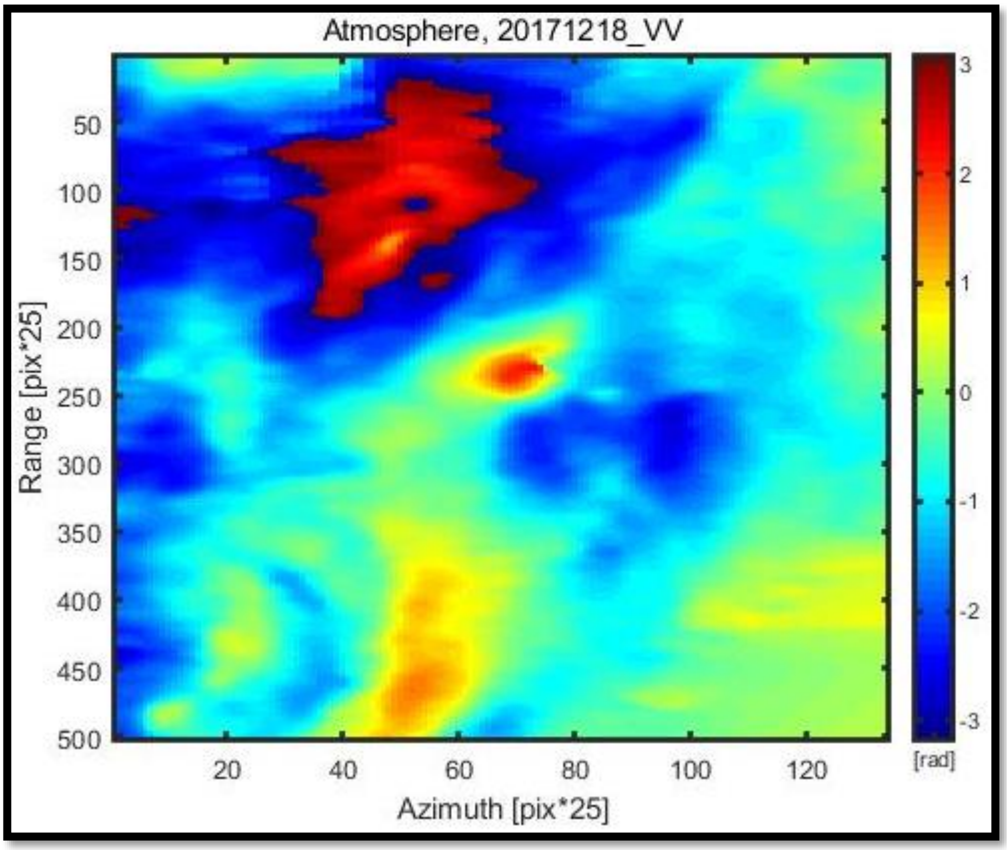
Atmosphere, 20171218_VV
Range [pix*25]
50
100
150
200
250
300
350
400
450
500
20
40
60
80
100
120
Azimuth [pix*25]
3
2
1
0
-1
-2
-3
[rad]

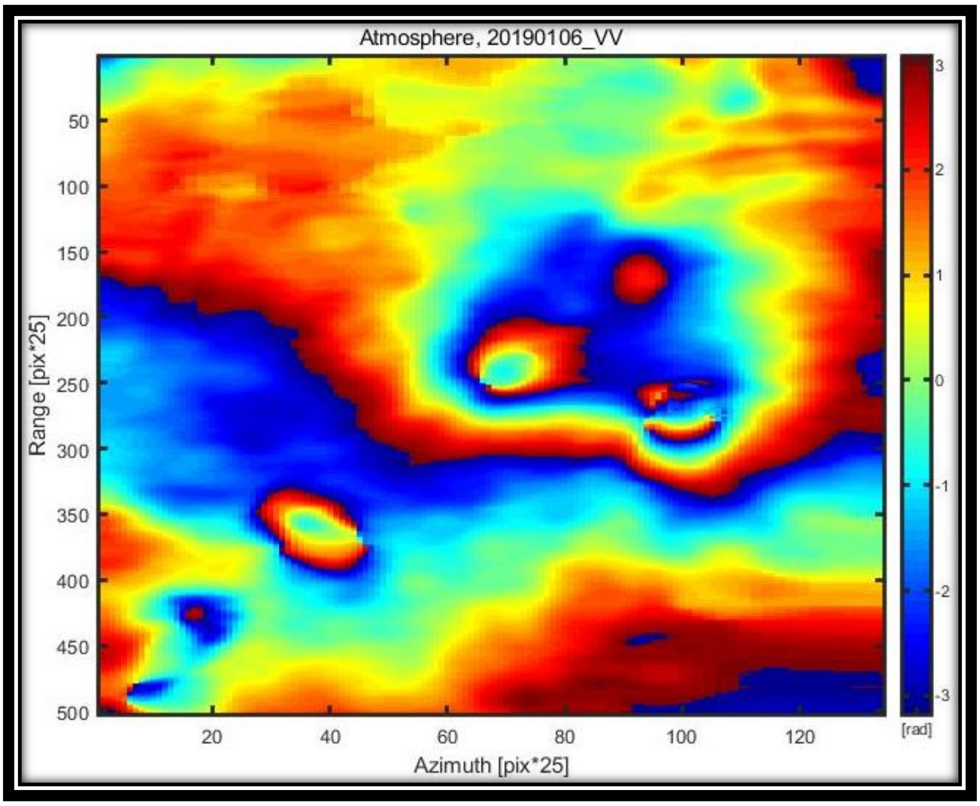
Atmosphere, 20190106_VV
Range [pix*25]
50
100
150
200
250
300
350
400
450
500
20
40
60
80
100
120
Azimuth [pix*25]
3
2
1
0
-1
-2
-3
[rad]

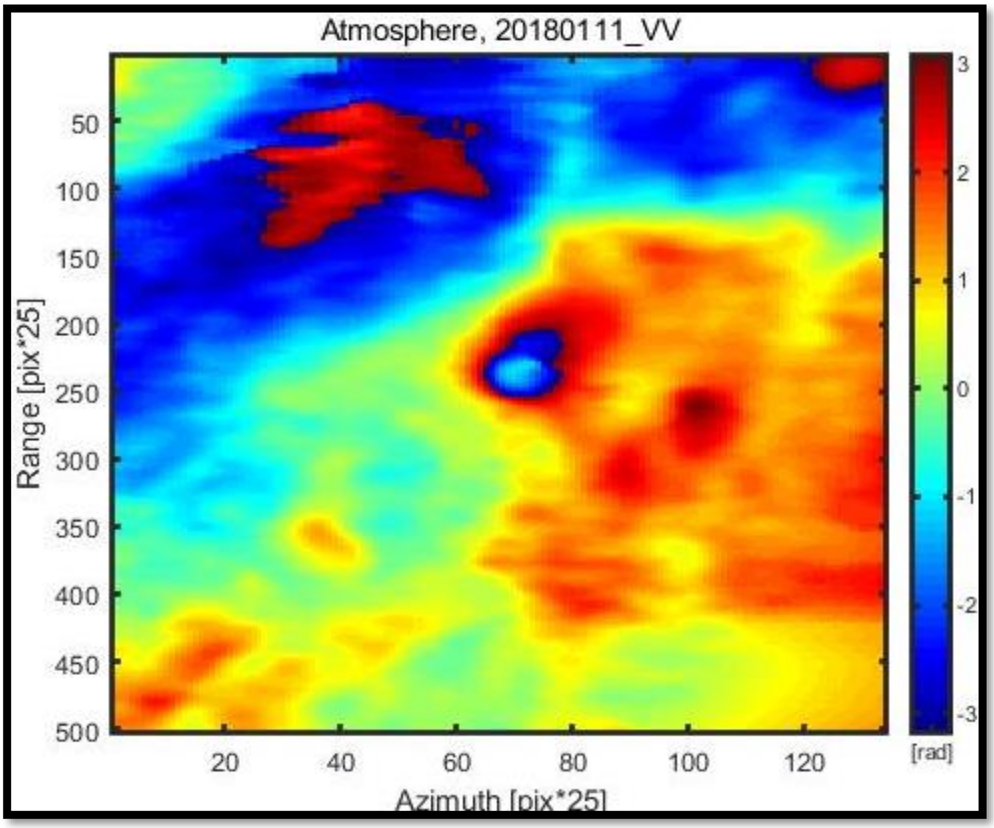
Atmosphere, 20180111_VV
Range [pix*25]
Azimuth [pix*25]
[rad]

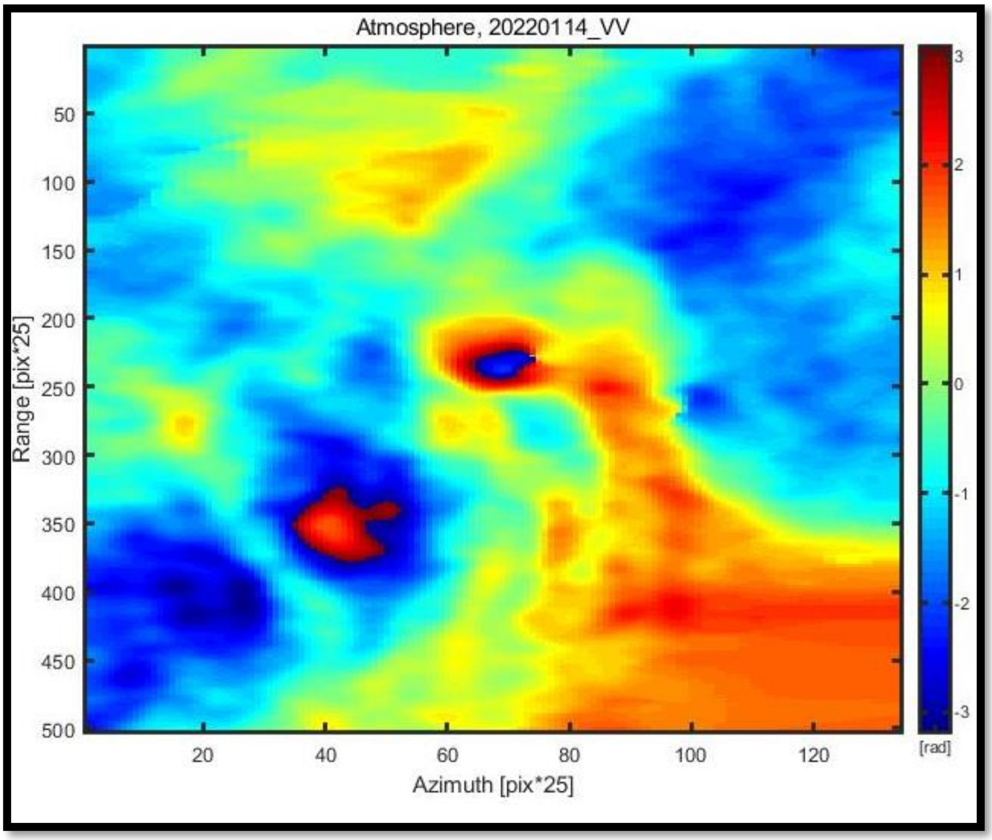
Atmosphere, 20220114_VV
Range [pix*25]
Azimuth [pix*25]
[rad]